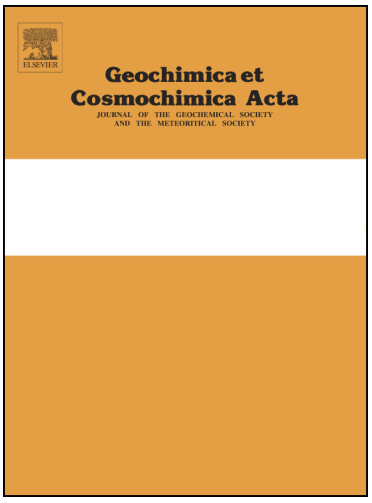

Diamondiferous Paleoproterozoic mantle roots beneath Arctic Canada: A study of mantle xenoliths from Parry Peninsula and Central Victoria Island

Jingao Liu, Laura E. Brin, D. Graham Pearson, Lisa Bretschneider, Ambre Luguet, David van Acken, Bruce Kjarsgaard, Amy Riches, Aleksandar Mišković

PII: S0016-7037(18)30438-1
DOI: https://doi.org/10.1016/j.gca.2018.08.010
Reference: GCA 10883

To appear in: *Geochimica et Cosmochimica Acta*

Received Date: 23 February 2018
Revised Date: 4 August 2018
Accepted Date: 6 August 2018

Please cite this article as: Liu, J., Brin, L.E., Graham Pearson, D., Bretschneider, L., Luguet, A., van Acken, D., Kjarsgaard, B., Riches, A., Mišković, A., Diamondiferous Paleoproterozoic mantle roots beneath Arctic Canada: A study of mantle xenoliths from Parry Peninsula and Central Victoria Island, *Geochimica et Cosmochimica Acta* (2018), doi: https://doi.org/10.1016/j.gca.2018.08.010

Diamondiferous Paleoproterozoic mantle roots beneath Arctic Canada: A study of mantle xenoliths from Parry Peninsula and Central Victoria Island

Jingao Liu[1,2]*, Laura E. Brin[2], D. Graham Pearson[2], Lisa Bretschneider[3€], Ambre Luguet[3], David van Acken[3§], Bruce Kjarsgaard[4], Amy Riches[2£], Aleksandar Mišković[5@]

[1]State Key Laboratory of Geological Processes and Mineral Resources, China University of Geosciences, Beijing 100083, China

[2]Department of Earth and Atmospheric Sciences, University of Alberta, Edmonton T6R3R4, Canada

[3]Steinmann-Institut für Geologie, Mineralogie und Paläontologie, Universität Bonn, Poppelsdorfer Schloss, 53115 Bonn, Germany

[4]Geological Survey of Canada, 615 Booth Street, Ottawa, Ontario K1A 0E9, Canada

[5]Northwest Territories Geological Survey, Yellowknife, NWT X1A 1K3, Canada.

*Corresponding author: jingao@cugb.edu.cn

€Now at GEOMAR, Helmholtz-Zentrum für Ozeanforschung, Kiel, Germany

§Now at iCRAG - Irish Centre for Research in Applied Geosciences, University College Dublin, Dublin, Ireland

£Now at School of Geographical and Earth Science, University of Glasgow, Glasgow, Scotland, United Kingdom

@ Now at GeoTarget Solutions Inc. Burnaby, BC, Canada

Revision to *Geochimica et Cosmochimica Acta*

August, 2018

ABSTRACT

While the mantle roots directly beneath Archean cratons have been relatively well studied because of their economic importance, much less is known about the genesis, age, composition and thickness of the mantle lithosphere beneath the regions that surround the cratons. Despite this knowledge gap, it is fundamentally important to establish the nature of relationships between this circum-cratonic mantle and that beneath the cratons, including the diamond potential of circum-cratonic regions. Here we present mineral and bulk elemental and isotopic compositions for kimberlite-borne mantle xenoliths from the Parry Peninsula and Central Victoria Island, Arctic Canada. These xenoliths provide key windows into the lithospheric mantle underpinning regions to the North and Northwest of the Archean Slave craton, where the presence of cratonic material has been proposed. The mantle xenolith data are supplemented by mineral concentrate data obtained during diamond exploration. The mineral and whole rock chemistry of peridotites from both localities is indistinguishable from that of typical cratonic mantle lithosphere. The cool mantle paleogeotherms defined by mineral thermobarometry reveal that the lithospheric mantle beneath the Parry Peninsula and Central Victoria Island terranes extended well into the diamond stability field at the time of kimberlite eruption, and this is consistent with the recovery of diamonds from both kimberlite fields. Bulk xenolith Se and Te contents, and highly siderophile element (including Os, Ir, Pt, Pd and Re) abundance systematics, plus corresponding depletion ages derived from Re-Os isotope data suggest that the mantle beneath these parts of Arctic Canada formed in the Paleoproterozoic Era, at ~2 Ga, rather than in the Archean. The presence of a diamondiferous Paleoproterozoic mantle root is part of the growing body of global evidence for diamond generation in mantle roots that stabilized well after the Archean. In the context of regional tectonics, we interpret the highly depleted mantle compositions beneath both studied

regions as formed by mantle melting associated with hydrous metasomatism in the major Paleoproterozoic Wopmay-Great Bear-Hottah arc systems. These ~2 Ga arc systems were subsequently accreted along the margin of the Slave craton to form a craton-like thick lithosphere with diamond potential thereby demonstrating the importance of subduction accretion in building up Earth's long-lived continental terranes.

Keywords: Mantle; Diamond; Osmium isotopes; Highly Siderophile Elements; Proterozoic; Craton

1. Introduction

The longevity, cool geotherm and sufficiently reduced oxidation state of cratonic lithosphere (e.g., Boyd and Gurney, 1986; Stagno et al., 2013) permits diamond crystals to grow and be preserved, making Archean cratons sampled by deeply derived volcanic rocks (e.g., kimberlites) key targets for diamond exploration. Since circum-cratonic lithosphere beneath Proterozoic or younger terranes has been traditionally thought to be thinner and thermally hotter than Archean cratons (Boyd and Gurney, 1986), these regions have not attracted as much attention from diamond explorers despite seismological evidence that the lithosphere can be as thick as or thicker than beneath the cratons (van der Hilst et al., 1998). The world-class Argyle diamond deposit is located in an early Proterozoic mobile belt on the margin of the Kimberley craton (e.g., Jaques et al., 1989), however, its lithospheric mantle root is clearly cratonic in origin (Luguet et al., 2009). Whether macrodiamonds commonly form in Proterozoic and younger lithosphere remains unclear, although diamond forming events of these ages are well established (e.g., Gurney et al., 2010).

Mantle peridotite xenoliths recovered from the kimberlite fields of the Parry Peninsula, Northwest Territories and Central Victoria Island, Nunavut in Northern Canada (**Fig. 1**) provide a precious opportunity to examine the nature of the circum-cratonic lithosphere to the North and Northwest of the Slave craton and to assess and understand its diamond potential. Although there are no extant outcrops of Archean crust found within the Parry Peninsula area, the region has been named as the "Mackenzie craton" by some workers (Davies and Davies, 2013) due to the presence of diamondiferous kimberlites in Darnley Bay area and the area north of Great Bear Lake, and associated abundant diamond-indicator minerals (e.g., garnet, chromite and ilmenite) that are indicative of diamond potential. The existence of this 'hidden' craton is additonally

supported by the finding of high seismic velocities beneath this area (Schaeffer and Lebedev, 2014). However, while high seismic velocity is consistent with a highly depleted cratonic-like mantle chemistry, it does not necessarily imply an Archean age.

The Central Victoria Island kimberlite field is known to contain diamondiferous kimberlites (Kolebaba et al., 2003). Whether the lithosphere beneath this area is Archean or not is contentious (e.g., Bleeker, 2003) due to the finding of a single Archean U-Pb zircon age of 2601± 3 Ma, obtained from granitoid rocks to the East at the Wellington Inlier (LeCheminant et al., 1996). It is important to address the question of whether Archean cratonic mantle, as a northerly extension of the Slave craton or as an independent cratonic fragment, underpins the Parry Peninsula and the Central Victoria Island regions and to assess the possible importance of such mantle for diamond potential.

Answering these key questions relies on determining the timing of lithospheric mantle stabilization. The Re-Os isotopic system has long-proven to be effective in dating melt depletion events of mantle peridotites (e.g., Walker et al., 1989; Pearson et al., 1995; Shirey and Walker, 1998; Pearson, 1999; Irvine et al., 2003; Carlson et al, 2005; Rudnick and Walker, 2009; Liu et al., 2010, 2011; Luguet et al., 2015). However, this isotopic system is not immune to the alteration by metasomatism and refertilization (e.g., Alard et al., 2002, 2011; Ionov et al., 2006; Luguet et al., 2007, 2015; Rudnick and Walker, 2009; van Acken et al., 2017). Given that Re and Os are primarily hosted by base metal sulfides (BMS) and platinum group minerals (PGM) in mantle lithologies, the element systematics including the highly siderophile elements (HSE here including Os, Ir, Ru, Pt, Pd and Re), Se and Te, particularly their ratios such as Pd/Ir and Se/Te can be utilized to trace the signature of metasomatic overprintings and evaluate the potential impact on the Os isotopic system (Luguet et al., 2001, 2003, 2004, 2015; Lorand et al., 2003;

Alard et al., 2002, 2011; Ackerman et al., 2009, 2016; van Acken et al., 2010a, b; ; Liu et al., 2010, 2015, 2016; König et al., 2014; Lorand and Luguet, 2016). In this paper, we combine petrology, mineralogy and chemistry including HSE, Se, Te abundances and Os isotopic compositions of peridotite xenoliths and concentrate minerals from Parry Peninsula and Central Victoria Island (**Fig. 1**), in order to determine the formation age, composition, geotherm and hence the likely thickness of the mantle lithosphere beneath these two localities. This new information provides fresh insights into the nature of the lithospheric mantle in these regions, its role in diamond mineralization over geological time, and its importance for understanding of the formation of Earth's continents.

2. Geological setting

Northern Canada is a complex patchwork of Archean cratons stitched together by Proterozoic suture zones that have been coherent blocks since 1.7 Ga (Hoffman, 1989). The Parry Peninsula and Central Victoria Island regions lie to the Northwest and North of the Archean Slave craton that has been well investigated through diamond exploration and exploitation (**Fig. 1**; e.g., Griffin et al., 1999; Aulbach et al., 2004a, 2011; Heaman and Pearson, 2010). The western margin of the Slave craton is a succession of North-South trending belts accreted to the craton during the Proterozoic. Its key component is the Wopmay orogen (1.91-1.70 Ga) including the collisional arc Hottah terrane and the Great Bear magmatic zone (1.88-1.86 Ga; Bowring and Podosek, 1989; Hoffman, 1989; see details of the tectonic subdivisions in Figure 1 of Ootes et al., 2015).

The Parry Peninsula region, Northwest Territories (**Fig. 1**), has been a center of mineral and diamond exploration since the 1950s; however, very little is known about the area in terms of geology, as the surface is dominated by sedimentary cover. This area was originally explored

due to the presence of a large geophysical anomaly: the Darnley Bay Anomaly, which is the largest gravity anomaly in North America (Hornal, 1970; Stacey, 1971), originally interpreted as a basic or ultrabasic intrusion lying beneath the Proterozoic and Paleozoic sediments. This anomaly differs in magnitude and shape from other gravity anomalies in the Mackenzie Basin, such as the Mackenzie River Anomaly and Fort Simpson Anomaly, which are related to early Proterozoic magmatic arcs (Pilkington and Saltus, 2009). Analysis of aeromagnetic data revealed discrete circular anomalies, resulting in the subsequent discovery of diamondiferous kimberlites in the Paulatuk area (**Fig. S1** in the **Electronic Annex**). The Parry Peninsula region is far from any recognized cratonic crustal blocks (Bleeker, 2003).

The supracrustal geology of Victoria Island, Nunavut, is comprised mostly of Paleozoic platform carbonate units, with occasional inliers of Paleoproterozoic basement rocks (Campbell, 1981), and Mackenzie dykes (1270 Ma) and basaltic magmatism of the Franklin event (723 Ma; Heaman et al., 2003). Archean rocks are scarce, with the only Archean age of 2.6 Ga from a granitoid located at Wellington Inlier (LeCheminant et al., 1996), and in the Hadley Bay area – a pink "Slave" granite that is cross-cut by a granodiorite dated at ca. 2.4 Ga (Thorsteinsson and Tozer, 1962). The tectonic provenance of Central Victoria Island is unclear as no Archean shield is well exposed; Bleeker (2003) and Kolebaba et al. (2003) denote this area as a possible northern extension of the Slave craton, however, no published data exist to support this suggestion. Victoria Island kimberlites occur along a strong NW-SE trending parallel dyke array comprising four main groups: the Galaxy structure, the Blue Ice trend, the Snowy Owl trend and the King Eider trend (**Fig. S2**). Of the kimberlites explored in the latter two trends, 80% have been found to be diamondiferous (Diamonds North press statement (DNR), 2006).

3. Samples and methods

3.1 Mantle xenoliths

Peridotite xenoliths from the Parry Peninsula (PP) were collected from drill core samples of the Darnley Bay kimberlites (dated at 270 Ma; Heaman et al., 2003) donated by Darnley Bay Resources Ltd. Fifteen peridotite xenoliths were recovered, ranging in weight from 3 to 302 g. The fresh nature of these samples permitted olivine mineral separates as well as whole rock powders to be prepared for elemental and isotopic analysis. Ten samples were prepared to make thin sections.

Central Victoria Island (CVI) xenoliths for this study were extracted from 22 drill cores of the Snowy Owl kimberlite (dated at 271 Ma; Heaman et al., 2003) donated by Diamonds North Ltd. The extracted xenoliths (n = 36) range in size from 1 to 8 cm and in weight from less than 1 to 76 g. Fifteen samples were selected for further analysis based on size, minimal kimberlite contamination and degree of alteration. Where present, garnet and olivine grains were isolated for mineral mounts; three samples (SnO-1, SnO-5 and SnO-34) were large enough to prepare thin sections.

3.2 Sample preparation

Peridotite xenoliths were removed from core using a combination of a MK660 saw, Isomet slow speed saw, and a hammer. All sawn edges were abraded with silicon carbide paper to remove saw marks and possible contamination. After being rinsed using deionized water, coarse crush was obtained by isolating small volumes of dry rock in plastic that were then broken with a hammer, and any residual kimberlite material, altered rims and vein fillings were carefully removed. Small volumes of the fine crush were then powdered in an alumina

ball mill or by hand in an agate mortar and pestle. Mineral separates were hand-picked and rinsed before being mounted or being used for isotope chemistry (i.e., olivine grains).

3.3 Analytical methods

3.3.1 Electron microprobe

Major element mineral analysis was performed at the University of Alberta using a CAMECA SX100 or a JEOL 8900R electron microprobe, on both thin sections and mineral mounts. Wavelength dispersive spectroscopy (WDS) was employed, at an accelerating voltage of 20 kV, a beam current of 20 nA and beam diameter of 3 microns. A variety of natural minerals (silicate and oxide) were used for standardization. Data reduction was performed using a ZAF correction along with lower limit of detection filters following the method of Potts (1992).

3.3.2 Trace element determinations

Trace element concentrations in garnet were determined by LA-ICP-MS at the University of Alberta, using a RESOnetics Resolution LR50 193nm laser coupled to a ThermoScientific Element 2XR ICP-MS. Spot sizes of 75µm were ablated at 10Hz repetition for 60 seconds with a laser energy of 120 mJ at 11.4 % attenuation. Concentrations were calculated with reference to the NIST612 glass standard using the Iolite data reduction program (Paton et al., 2011; https://iolite-software.com/). Secondary standards (BIR-1G standard, and natural in-house garnet megacrysts PN1, PN2; **Electronic Annex**) were also measured to monitor accuracy. For internal standardization, garnet trace element concentrations are normalized to Ca in case of rare earth elements (REEs) and Si for transition metals (Ni, Ti). The elemental concentrations determined for the secondary standards

(i.e., BIR-1G, PN1 and PN2) agree with the recommended values within relative errors of typical 4–8% or better at the 95% confidence level.

3.3.3 X-ray fluorescence

Whole-rock major element compositions as well as loss-on-ignition (LOI) values were measured using X-ray Fluorescence (XRF) at Franklin & Marshall College, United States, on ~2.5 g aliquots of homogenized sample powders following the protocols of Boyd and Mertzman (1987). The international reference material harzburgite MUH-1 was analyzed during the analytical campaign, and the results show that analytical precision and accuracy for major elements was typically better than 5%.

3.3.4 Re-Os isotope, highly siderophile element (HSE), Se and Te abundances

All HSE abundances and Re-Os isotopic compositions were determined at the University of Alberta using isotope dilution techniques modified after Pearson and Woodland (2000). Approximately 1g of whole rock powder, or hand-picked olivine separates was digested, along with a mixed HSE spike (^{99}Ru, ^{106}Pd, ^{185}Re, ^{190}Os, ^{191}Ir and ^{194}Pt), with inverse *aqua regia* (2.5mL 10 N HCl : 5mL 14 N HNO_3) for 16 hours at 290°C and approximately 130 bars in a high pressure asher (HPA-S, Anton Paar). Osmium was separated from the other HSEs using chloroform and 9N HBr before microdistilling to purify the Os fraction. The purified Os fraction was then loaded onto a platinum filament using 9N HBr, with a $NaOH\text{-}Ba(OH)_2$ activator. Osmium was measured on a Thermo Triton Plus N-TIMS (negative thermal ionization mass spectrometer) using the axial SEM in a peak-hopping mode. Osmium isotope compositions are corrected for mass-dependent isotope fractionation and oxygen isotope

interferences. SEM yield and long-term performance of the instrument were monitored using 250 pg loads of a Durham Osmium Standard (DROsS; $^{187}Os/^{188}Os$ = 0.16078 ± 0.00024; 2σ; n = 52; Liu and Pearson, 2014) that yielded ion beams of similar sizes to most peridotites and olivine separates analyzed here, and the results are in excellent agreement with the original determination of the DROsS value by NTIMS on 10-100 ng aliquots (0.160924±0.000004; 2σ; Luguet et al., 2008).

The other HSEs were isolated through anion-exchange chromatography columns using AG1X8 resin (100-200 mesh). The resulting solutions were measured on a Thermo Element XR2 ICP-MS using a Peltier-cooled micro-concentric nebulizer. Solutions of 1ppb in-house standards for each target element were analyzed to measure and correct for instrumental mass bias. Before each run, molecular oxide interferences (e.g., YO^+, ZrO^+, MoO^+, HfO^+, YbO^+) were determined to perform offline oxide interference corrections. HSE solutions of 1 ppb were prepared using 0.8N HNO_3 except for Pd where 1N HCl was employed to more efficiently retain Pd in solution. Results were corrected for background and molecular oxide isobaric interferences before isotope dilution calculations were performed. The Beni Bousera peridotite GP-13 was determined repeatedly during the analytical course and used as our in-house reference standard for peridotite matrix. The results of GP-13 agree well with accepted values.

Duplicate analyses of HSEs as well as Se and Te concentrations were performed on the same whole-rock powder aliquots at the Steinmann Institute, Universität Bonn. The details of chemical protocols are provided in Luguet et al. (2015) and references therein. About 1 g of sample powders were weighed together with spikes (^{77}Se, ^{99}Ru, ^{106}Pd, ^{125}Te, ^{185}Re, ^{191}Ir and ^{194}Pt) and 7.5 mL *inverse* aqua regia into a quartz vial and were digested for 13.5 hours at

220°C and 110-130 bars in a HPA-S. After digestion, the solutions were split half-half to conduct HSE and Se-Te chemical procedures separately. The aliquots for HSE measurements were dried down, treated with HNO_3-HF to ensure a complete recovery for Re and finally converted to HCl solution for purification of HSE via anion column chromatography. The Se-Te chemistry used the protocol of Wang and Becker (2014) which employs a combination of anion and cation resin procedures. All HSE-Se-Te measurements were conducted using a Thermo Element XR2 ICP-MS. In this analytical campaign, reference material UB-N was analyzed in order to check the reproducibility and accuracy of the measurements, and the results of UB-N agree well with accepted values.

4. Petrology and mineralogy of the mantle peridotites

4.1 Petrography

4.1.1 Parry Peninsula peridotites

The Parry Peninsula (PP) peridotites are all spinel-facies, coarse-equant harzburgites or lherzolites (classification scheme of Harte, 1977) with curving, granuloblastic grain boundaries (**Fig. S3**). Strain is visible in thin section as undulose extinction and sub-grain formation. Coarse equant samples were generally fresh. The high-strain samples are more altered, but still have LOI values < 8 wt. %. Spinel symplectite textures are present in association with orthopyroxene, most likely resulting from garnet breakdown (**Fig. S3**; e.g., Medaris et al., 2005).

Olivines are coarse (0.5-10 mm), exceptionally fresh, with vitreous surfaces, and range from light green to colorless. Some olivines contain inclusions of chromite. The majority of samples are slightly altered along fractures in the olivine (**Fig. S3**). Orthopyroxenes are tabular, light brown and on average l mm in size. In thin section, they display minor clinopyroxene exsolution.

Clinopyroxenes (Cr- diopside), a minor phase in the peridotites, are irregular and can be found at grain boundaries (0.5-2 mm) between olivine and orthopyroxene. They are typically found in association with irregular aluminous spinel grains (up to 1.5 mm), that also display irregular grain shapes.

4.1.2 Central Victoria Island peridotites

The Central Victoria Island (CVI) peridotites are coarse-grained garnet lherzolites, with equigranular textures. The majority (n = 30) display intense serpentinization: garnet is the only mineral to escape complete replacement. While serpentinized minerals are chemically indistinguishable, primary grain boundaries are highlighted by dark serpentine veining (**Fig. S4**). Garnets are variable in size (<1-5 mm, average ~1 mm) and color (from dark red, light pink to medium purple). These garnet grains display kelyphite rims and are generally rounded or with rare irregular shapes. In some samples, garnets form clusters up to 12 mm across. Secondary chromites, associated with recrystallization of the kelyphite alteration rims, are equant, euhedral, fine-grained (1-200 µm), and magnesium-rich**.** The other 6 peridotite xenoliths show more complex alteration. They contain rare grains of fresh olivine: relics of larger grains were found and recovered for analysis, typically <100 µm in size. Pyroxenes have been completely replaced but still display primary grain boundaries and interference colors that distinguish them from olivine. Garnets are on average larger (1-5 mm, average ~2 mm) and are typically light pink to medium purple. Spinels are dark red-brown in color, with straight grain boundaries, that are intergrown with olivine and orthopyroxene, sometimes as inclusions.

4.2 Mineral chemistry

4.2.1 Xenoliths

Olivine: Within the PP peridotites (**Table S1a** in the **Electronic Annex**), their forsterite contents (Fo, i.e., magnesium number Mg#= molar [Mg/(Mg+Fe)]x100) range from 91.9 to 92.6 with a mean of 92.2 ± 0.5 (n = 14; 2σ here and elsewhere unless specified). Five CVI peridotites containing relic olivine display a range of Fo from 91.7 to 92.4 (mean = 91.9 ± 0.6; n = 5). The olivine compositions from both localities are similar to the published olivine Fo values obtained from Archean peridotites of the central Slave craton (90.5-92.8; Pearson et al., 1999) and Kaapvaal craton (mean Fo = 92.5 ± 1.3; Pearson and Wittig, 2008), as well as the Greenland cratonic peridotites (91.5-93.0; Bernstein et al., 1998, 2006; Sand et al, 2009; **Fig. 2**). On the other hand, these Fo values are statistically higher on average than those reported for South African off-craton peridotites (mean = 91.4±1.1; Boyd et al., 2004; Janney et al., 2010).

Clinopyroxene: Fresh Cr-diopsides are found only in the PP peridotites. They have a small compositional range (Mg#s of 95.4-96.2) with low TiO_2 (<0.03 wt. %) and NiO contents (up to 0.06 wt. %; **Table S1a**). While the low TiO_2 concentrations are consistent with values reported for the Slave craton (e.g., Kopylova et al., 1999; Pearson et al., 1999; Kopylova and Caro, 2004), the Mg#s are much higher, consistent with their low equilibration temperatures (see below).

Orthopyroxene: The PP orthopyroxenes show similar trends in Mg# (92.4-92.9) and minor oxides (TiO_2 up to 0.02 wt. %; NiO up to 0.09 wt. %; **Table S1a**) as the Cr-diopsides. They have low Cr_2O_3 and CaO contents (mean = 0.31 wt. % and 0.27 wt. %, respectively) and a large range in Al_2O_3 contents (0.86 to 3.26 wt. %). Mg#s and Cr_2O_3 concentrations are consistent with values reported for Slave craton peridotitic orthopyroxenes, while CaO

contents are lower or similar (Kopylova et al., 1999; Pearson et al., 1999), also consistent with their low equilibration temperatures.

Spinel: The PP lherzolites have spinel grains that are Cr-rich (25.4-48.4 wt. % Cr_2O_3) with Cr# (molar Cr/(Cr+Al) x 100 = 32 to 60 (**Table S1a**; **Fig. 2**). Spinels are found in only two CVI peridotites (SnO-1 and SnO-5). In sample SnO-1, spinels display a range of Cr_2O_3 and Al_2O_3 contents, 21.2 to 42.2 wt. % and 22.6 to 44.1wt. %; respectively; average Cr# is 43.8. Spinels from SnO-5 are much higher in Cr_2O_3 (59.0-59.4 wt. %) and lower in Al_2O_3 (9.3-9.8 wt. %); average Cr# equals to 80.6 (**Table S1b**). In both samples, the spinels are euhedral and spatially associated with garnet grains.

Garnet: Only one sample (DB2D) from Parry Peninsula contains both spinel and garnet, and the garnet has a Cr_2O_3 content of 1.76 wt. % and CaO content of 5.34 wt. % (**Table S1a**). Garnets from the CVI xenoliths are chromium pyropes with Cr_2O_3 contents of 2.15 to 9.32 wt. % (mean = 6.11 wt. %) and CaO contents between 4.10 and 7.02 wt. % (mean=5.68 wt. %) (**Table S1b**). Based on the criteria of Gurney (1984) and Grütter et al. (2004), the majority of the CVI garnets are classified as calcic-lherzolitic G9 (**Fig. 3A**). Their TiO_2 contents are variable within the suite (ranging from below detection limit to 0.64 wt. %, mean = 0.13 wt. %).

4.2.2 Concentrate mineral chemistry

In addition to the PP xenoliths, comparative data for kimberlite indicator minerals analyzed by Energy Dispersive Spectrometry (EDS) are available for the Darnley Bay exploration property through the GoData kimberlite indicator mineral database maintained by the Northwest Territories Geological Survey. Additional concentrate mineral major element data for the Central Victoria Island kimberlite field came from various sources. Concentrate

minerals from the Snowy Owl kimberlite were provided by Diamonds North Resources Ltd., using materials used in their exploration campaign. All data from other kimberlites in the Snowy Owl trend were obtained from Monopros (DeBeers) internal reports. CVI indicator mineral mounts from kimberlites in the other trends were provided by DeBeers, along with the associated garnet, clinopyroxene and spinel separate grains (**Table S2a-h**). All previous data were acquired in EDS mode, while new WDS major element analyses as well as laser ablation trace element work were performed on available grain mounts (**Table S2a,b**; e.g., **Figs. S5, S6**). On average, EDS and WDS data plot close to 1:1 lines except for minor elements such as Na in pyroxene which is systematically displaced to lower values in the EDS data. In general though, the close agreement of WDS and EDS data for most major elements supports the use of the EDS data for qualitative assessment with respect to the xenolith WDS data.

Garnet: The garnet concentrate data from glacial till (**Table S2c**; n = 3244) across the Central Victoria Island kimberlite fields display a dominant peridotitic component (82 % lherzolitic G9 and 4 % harzburgitic G10 including 6 grains accounting for ~0.2 % of the population that classified as G10D). In addition, strong pyroxenitic (dominantly G4) and eclogitic (dominantly G3) components are present, accounting for 14 % of the total grains **(Fig. 3**A), higher than the ~ 4 % of eclogites in the garnet-bearing mantle of the neighboring central Slave craton (McLean et al., 2007). The variable eclogitic contents between kimberlite pipes suggest that kimberlites along the four distinct structural trends sampled different proportions of the various lithologies in the mantle columns. Garnets from both the peridotite xenoliths and mineral concentrate have CaO and Cr_2O_3 contents that are similar to contents previously reported for cratonic garnets from the central Slave craton, the Kaapvaal craton and circum-cratonic Kaapvaal sources (e.g., Kopylova et al., 1999; Grégoire et al., 2003; Simon et

al., 2003; Janney et al., 2010).

Data for garnets derived from glacial till in Parry Peninsula (**Table S2d**; n=872) indicate a mantle lithosphere composition that is dominantly peridotitic (97 % peridotitic and 3% eclogitic), with predominant "lherzolitic" G9 garnets and a subset of only 3 grains barely projecting into the G10D compositional field (**Fig. 3**B).

Clinopyroxene: Till concentrate clinopyroxenes from both CVI (**Table S2e**; n =1063) and PP (**Table S2f**; n=524) have overlapping compositions characterized by lower Mg#s (82-95) and generally much higher TiO_2 concentrations (0.01-0.42 wt. %, mean=0.21 wt. %) than those from the PP xenoliths. They appear broadly cratonic in composition (**Fig. 3**C).

Spinel: Till concentrate spinels from CVI (**Table S2g**; n =36) are characterized by extremely high Cr# and relatively low Mg#, while those from PP (**Table S2h**; n = 744) have a broader spread in compositions extending to higher Cr# and lower Mg# than the xenolith spinels. Both till concentrate and xenolith spinels from both localities have compositions largely plotting within the cratonic peridotite field, although the xenolith spinels also overlap with the non-cratonic peridotitic spinels (**Fig. 3D**).

4.3 Garnet trace element chemistry

4.3.1 Xenoliths

Xenolith-derived garnets from Central Victoria Island display high Ni contents (38-162 ppm; n=15) with more than 75 % of the data clustering between 50-70 ppm (**Table S3a**). They display four distinct types of rare earth element (REE) patterns (**Fig. 4A**). Type 1 garnets (SnO-19 and SnO-20) have very low LREE concentrations, increasing to chondritic abundances through the MREEs to 10x chondritic in the HREEs. This pattern is typical for

fertile lherzolitic garnets (e.g., Stachel et al., 1998; Pearson et al., 2003). In contrast, Type 2 garnets (SnO-15, SnO-26 and SnO-32) have variable LREE abundances that are near chondritic, with decreasing concentrations from Nd to Tb but increasing REE concentrations through the HREE with chondritic concentrations towards Lu. Moreover, Type 3 garnets (SnO-11, SnO-12, SnO-17, SnO-24, SnO-28 and SnO-35) display a sinusoidal trend that is characterized by a peak within the LREE around Nd or Sm and a minimum at Tb to Tm through the MREE to the HREE. Such sinusoidal patterns are typically seen in harzburgitic garnets (e.g., Shimizu and Richardson, 1987; Stachel et al., 1998; Aulbach et al., 2004b). Both type 2 & 3 garnet REE patterns are usually observed in cratonic peridotite suites (e.g., Stachel et al., 1998; Simon et al. 2003; Shu and Brey, 2015). Type 4 garnets (SnO-33 and SnO-34) have near constant positive slope from Ce to Lu that is different from all other garnet patterns but intermediate in between Type 1 and Type 3 patterns.

4.3.2 Concentrate garnet

Trace elements were analyzed for 55 garnet concentrate grains from Central Victoria Island kimberlites (**Table S3b**). Nickel concentrations in the concentrate garnets are somewhat lower than those determined for the xenolith garnets (12-87 ppm, n=55). Using the same trace element pattern classification developed for the xenolith garnets, there is a strong bias towards the lherzolitic, Type 1 garnet REE patterns, accounting for 45 % of the data and in agreement with the high lherzolitic garnet component estimated from major element data (**Fig. 4B**). Type 3 (sinusoidal) garnet patterns (49 %) are more common, while Type 2 garnet patterns represent only 5 % of the garnet concentrate grains (**Fig. 4C**). No Type 4 patterns were discovered in the concentrate garnets.

Consistent with having variable types of REE patterns, garnets from both xenoliths and till concentrate have large ranges of Zr (0.1-128 ppm) and Y (0.3-27 ppm) concentrations (**Table S3**; **Fig. 5A**). Furthermore, they also have chondritic to suprachondritic Zr/Hf ratios (32-107) and an extremely large range of Ti/Eu ratios from subchondritic to suprachondritic (360-39000) (**Fig. 5B**).

4.4 Bulk rock major element chemistry and modal mineralogy

Bulk rock major element compositions of the PP and CVI peridotites as well as reference material MUH-1 are provided in **Table S4**. Anhydrous whole rock MgO contents of the PP peridotites vary from 44.5 to 48.5 wt. %, whereas the CVI peridotites have lower MgO contents over a larger range (37.7 to 46.7 wt. %; **Table S4**). These ranges are comparable to both global cratonic peridotites (mean= 46.2 ± 2.9 wt. %; Pearson et al., 2003) and the neighboring central Slave cratonic peridotites (mean = 46.1± 2.1 wt. %; Aulbach et al., 2007) as well as Kaapvaal circum-cratonic peridotites (37 to 48 wt. %; Janney et al., 2010). CaO contents in the PP peridotites is very low and restricted to a narrow range (0.21-0.98 wt. %), similar to the most depleted cratonic peridotites such as those from the North Atlantic Craton (**Fig. 6**; Wittig et al., 2008). The low bulk rock Al_2O_3 (0.45-1.21 wt. %) is also comparable to cratonic peridotites (**Fig. 6**) and is lower than that measured in peridotites from Phanerozoic and Proterozoic rifts in young tectonic terranes (see compilation in Pearson et al., 2014 and Pearson and Wittig, 2014).

In contrast to the PP peridotites, CaO is highly variable in CVI peridotites (0.31-4.33 wt. %) extending from values typical of cratonic peridotites (e.g., Pearson et al., 2003) to much higher values that exceed the likely value for fertile mantle (~3.5 wt. %; McDonough and Sun,

1995). The four samples (SnO-12, SnO-15, SnO-21 and SnO-24) have the highest CaO contents (~ 4 wt. %) accompanied by elevated bulk rock Sr contents (>200 ppm), but have significantly lower Al_2O_3 contents, which resemble typical cratonic peridotites (**Fig. 6**). In addition, two samples (SnO-19 and SnO-20) containing phlogopite have higher Al_2O_3 (>3 wt. %) but relatively low CaO contents (<1.6 wt. %; **Fig. 6**).

Modal mineral proportions were calculated for the PP peridotites using whole rock compositions and the MINSQ program of Herrmann and Berry (2002). Representative mineral compositions for each xenolith were used for each calculation to ensure accuracy. While the samples are relatively small for this approach, potentially compromising accuracy, the resulting calculated modes confirm petrological indications that the peridotites are olivine rich, with olivine abundances between 73 to 89 vol. %, with the peridotite DB4B as low as 62 vol. % (**Table S4**; **Fig. 2**A). Modal orthopyroxene varies from 9 to 24 vol. % with one exception (DB4B; 35 vol. %). These orthopyroxene modes are similar to the range of 5-37 vol. % reported for the Slave cratonic peridotites (Aulbach et al., 2007), but higher than the most orthopyroxene-poor cratonic peridotites, typified by the North Atlantic craton (Wittig et al., 2008). As expected from their low Al and Ca contents, modal clinopyroxene is very low (0.01 to 3.75 vol. %; **Table S4**). Spinel modal abundances average <1 vol. % but are as high as 3 vol. % in the peridotite DB11A. No mineral modal abundances were calculated for the CVI peridotites due to their highly altered state and the lack of fresh mineral compositions, with the exception of garnet.

5. Highly siderophile elements, Se, Te and Re-Os isotope systematics

5.1 Highly siderophile elements, Se and Te systematics

Duplicate analyses of HSE for a subset of peridotites between the University of Alberta and Universität Bonn laboratories, generally show good agreement (**Table 1**; the data for the reference peridotites UB-N and GP-13 as well as blanks are provided in **Table S5**). The outliers can be interpreted as a result of nugget effects resulting from the relatively small powder aliquots analyzed. The Universität Bonn lab did not measure Os concentration or Os isotopic composition, while Ru was not determined at the University of Alberta due to interference problems.

Based on absolute HSE-Se-Te concentrations and HSE fractionations (**Fig. 7A**), the HSE systematics of CVI peridotites, expressed as CI-chondrite normalized patterns can be categorized into five subgroups (Group A to E) with key signatures summarized in **Table 2** and highlighted here. Group A including samples SnO-27 and SnO-32 are characterized by Os (4.8-7.3 ppb) and Ir (4.4-6.4 ppb) concentrations higher than primitive upper mantle (PUM; Becker et al., 2006), variable Se (below detection limit (2 ppb = 3σ of the average blank) and 7.4 ppb) and Te (0.9-9.5 ppb) contents, chondritic Os/Ir ratios (Os_N/Ir_N = 0.99-1.05, N: CI-chondrite normalization after Anders and Grevesse, 1989 and Horan et al., 2003), subchondritic Pt/Ir ratios (Pt_N/Ir_N = 0.57-0.63), and extremely low Pd/Ir ratios (Pd_N/Ir_N = 0.02-0.04),. Group B including samples SnO-12 and SnO-21 are characterized by PUM-like or slightly lower Os (2.4-3.9 ppb) and Ir (2.5-3.9 ppb) concentrations, Se (16.4 ppb for SnO-12 and not determined for SnO-21) and variable Te (4.8-15.7 ppb) contents, nearly chondritic Os/Ir ratios (both Os_N/Ir_N = 0.90), subchondritic Pt/Ir (Pt_N/Ir_N = 0.25-0.37) and Pd/Ir (Pd_N/Ir_N = 0.16-0.24) ratios. Group C including samples SnO-15, SnO-24 and SnO-33 are characterized by PUM-like or higher Os (3.5-7.1 ppb) and Ir (3.5-6.9 ppb) concentrations, variable Se (3.6-13.9 ppb) and Te (1.1-8.7 ppb) contents, subchondritic to

chondritic Os/Ir ratios (Os_N/Ir_N = 0.72-0.98), subchondritic Pt/Ir ratios (Pt_N/Ir_N = 0.46-0.82), subchondritic Pd/Ir ratios (Pd_N/Ir_N = 0.13-0.30). Group D including samples SnO-11, SnO-17, SnO-19, SnO-20, SnO-28, SnO-29, SnO-34 and SnO-35 are characterized by PUM-like or higher Os (2.8-5.3 ppb, up to 16.3 ppb) and Ir (2.2-4.9 ppb, up to 9.4 ppb), generally higher Se (14.5-25.9 ppb) and Te (0.8-11.9 ppb) contents than the other three groups, subchondritic to suprachondritic Os/Ir ratios (Os_N/Ir_N = 0.78-1.58), subchondritic to suprachondritic Pt/Ir ratios (Pt_N/Ir_N = 0.55-1.37), slightly subchondritic to suprachondritic Pd/Ir ratios (Pd_N/Ir_N = 0.70-1.33). Group E including samples SnO-26 and SnO-36 are characterized by Os (0.4-1.0 ppb) and Ir (1.8-2.3 ppb) concentrations significantly lower than PUM estimates, low Se (below detection limit) and Te (below detection limit and 3.8 ppb) contents, remarkable subchondritic Os/Ir ratios (Os_N/Ir_N = 0.18-0.50), subchondritic Pt/Ir (Pt_N/Ir_N = 0.02-0.19) and Pd/Ir ratios (Pd_N/Ir_N = 0.02-0.34). All five groups of CVI peridotites have subchondritic, variable Re/Ir ratios (Re_N/Ir_N = 0.03-0.92). Overall, the CVI peridotites show gradually less depletion of Pd relative to Ir from Group A to Group D, with Group D analogous to typical PUM-like patterns, whereas Group E exhibit considerably lower HSE concentrations with distinct Os depletion relative to Ir.

Of the PP peridotites, four samples (DB1A, DB3A, DB4B and DB6A) broadly fall into the CVI Group A or Group C and are characterized by variable Os (1.6-8.1 ppb) and Ir (1.1-3.3 ppb) concentrations, suprachondritic Os/Ir ratios (Os_N/Ir_N = 1.2-2.3), subchondritic to suprachondritic Pt/Ir (Pt_N/Ir_N = 0.7-2.3) and extremely low Pd/Ir ratios (Pd_N/Ir_N < 0.14) (**Fig. 7B**), whereas the remaining four peridotites (DB2D, DB3C, DB5C and DB8A) display HSE patterns akin to the CVI Group E and are characterized by extremely low Os (0.05-0.80 ppb) and moderately low to PUM-like Ir (0.34-3.80 ppb) concentrations, subchondritic Os/Ir ratios (Os_N/Ir_N = 0.15-0.84), subchondritic to suprachondritic Pt/Ir (Pt_N/Ir_N = 0.12-1.30) and extremely low Pd/Ir ratios

(Pd_N/Ir_N <0.12). In summary, although there are remarkable Os-Ir fractionations in the PP peridotites, their Pd/Ir ratios remain extremely low. In addition, hand-picked olivine separates of the PP peridotites show broadly similar HSE concentrations and patterns as their whole rock compositions with a few outliers again likely resulting from nugget effects of heterogeneously-distributed HSE-bearing trace phases (**Fig. 7**C).

HSE concentrations and elemental ratios (e.g., Os_N/Ir_N and Pd_N/Ir_N) of peridotites from both PP and CVI suites poorly correlate with the whole-rock lithophile major element compositions (e.g., Al_2O_3 and CaO; **Fig. 8A, B**) and garnet lithophile trace element concentrations or ratios. Osmium, Ir and Pt concentrations show overall positive correlations (R^2 > 0.71; **Fig. 8C, D**) suggesting the existence of common host phases for these elements, however, the correlation within each group is weak, implying the diversity and discrepancy of the host phases in different peridotites, for example the Group E peridotites whose HSE systematics were likely affected by the processes associated with Os depletion relative to Ir. Within each group of peridotites, Pt and Pd concentrations do not show a good correlation (R^2 = 0.18) indicating that Pt and Pd are not controlled by the same host phases, except for the Group D peridotites that instead show a positive correlation (R^2 = 0.92; **Fig. 8E**); similar correlations also appear between Pd_N/Ir_N, Pt_N/Ir_N and Pd_N/Pt_N (not shown) ratios (**Fig. 8F**) but exclusively again among Group D peridotites.

For the Se analysis, only 10 CVI peridotites (Groups A, B, C, D) yielded signals sufficient for accurate determination. The data show a broadly positive correlation between Al_2O_3 and Se (R^2 = 0.74; **Fig. S7A**). However, the correlation of Pd and Se is poor (R^2 = 0.02), although the Group D peridotites have overall higher Pd (**Fig. S7B**) or Pd_N/Ir_N (**Fig. S7C**) and Se concentrations than the other peridotites. For Te, the PP peridotites have low Te (0.4-2.1 ppb)

concentrations, systematically lower than those of the CVI peridotites (Te = 0.9-16.2 ppb). Tellurium concentrations (available for the full CVI sample suite) do not correlate well with Al_2O_3 (R^2 = 0.12; **Fig. S7D**) or Pt (R^2 = 0; **Fig. S7E**). Selenium and Te concentrations of the CVI peridotites are not well correlated (R^2 = 0.30; **Fig. S7F**). Overall, such complex HSE-Se-Te systematics in both the PP and CVI peridotites cannot have been produced solely by mantle melt depletion but also reflect the influence of later metasomatic overprints.

5.2 Re-Os isotope systematics

The PP whole rock peridotites have a narrow range in $^{187}Os/^{188}Os$ (0.1119-0.1162), while their olivine separates have broadly similar compositions but ranging to slightly more radiogenic values than their whole rocks (0.1119-0.1204). The limited range of $^{187}Os/^{188}Os$ values in the whole rock PP peridotites (**Fig. 9A**), define near horizontally trends against chemical indices, such as Al_2O_3 (**Fig. 9B**), CaO (**Fig. 9C**), Pd_N/Ir_N (**Fig. 9D**), 1/Os (**Fig. 9E**) and Os_N/Ir_N (**Fig. 9F**). Peridotite DB6A has a distinctively lower $^{187}Os/^{188}Os$ of 0.1119 than the other PP peridotites. Both whole rocks and olivine separates generally have strongly subchondritic Re/Os ratios ($^{187}Re/^{188}Os < 0.1$) when compared to the chondrites (~0.4; Horan et al., 2003), with peridotite DB2D having a higher value of 1.4. Most of the PP whole rocks plot near or along the 0.27 Ga (eruption age) reference isochron; in contrast, the olivine separates mostly plot near or along the 2 Ga reference isochron (**Fig. 10A**).

Although the CVI peridotites have a broader range of Os isotopic compositions extending to more radiogenic $^{187}Os/^{188}Os$ compositions (i.e., 0.1109-0.1246), there is a clear clustering of Os isotope compositions within the Group A, B, C and E peridotites (mostly 0.1136-0.1162, **Fig. 9A**), at values that are identical to the main range of the PP whole rock peridotites. Likewise,

despite showing a wider range in major element and HSE compositions, the $^{187}Os/^{188}Os$ ratios of these four groups of CVI peridotites do not show significant variations with indices commonly utilized to determine partial melting and melt/rock interaction, e.g., Al_2O_3 (**Fig. 9B**), CaO (**Fig. 9C**), Pd_N/Ir_N (**Fig. 9D**), 1/Os (**Fig. 9E**) and Os_N/Ir_N (**Fig. 9F**). Although these four groups of peridotites show a large range of $^{187}Re/^{188}Os$ ratios (0.02-0.31), they plot near or along the 0.27 Ga reference isochron. The CVI Group D peridotites are distinct from the above groups in that they show a much larger range of $^{187}Os/^{188}Os$ ratios (0.1144-0.1246) coupled with highly variable Al_2O_3 contents (1.1-4.6 wt. %) and high Pd_N/Ir_N ratios (0.69-1.35) relative to the other groups of CVI peridotites (Al_2O_3 = 0.7-2.0 wt. %; Pd_N/Ir_N = 0.02-0.36). Moreover, the CVI Group D peridotites show a positive correlation between $^{187}Os/^{188}Os$ and Pd_N/Ir_N (**Fig. 9D**), while their $^{187}Os/^{188}Os$ ratios show no covariations with 1/Os (**Fig. 9E**) or Os_N/Ir_N (**Fig. 9F**). In addition, five Group D peridotites display a positive correlation between $^{187}Os/^{188}Os$ and $^{187}Re/^{188}Os$ values, corresponding to a 3.8 Ga reference isochron, while the remaining two peridotites plot either along the 0.27 Ga reference isochron or close to the PUM estimate (**Fig. 10A**).

6. Discussion

Previous studies have shown that the chemical compositions of lithospheric mantle peridotites commonly result from multiple processes, including primary (partial melting and melt extraction) and secondary (metasomatism and/or refertilization) processes. Secondary processes can obscure the primary partial melting signature in cratonic peridotites (e.g., Luguet et al., 2001, 2003, 2015; Lorand et al., 2003a, b; Aulbach et al., 2016; Luguet and Reisberg, 2016 and references therein). Thus, it is necessary to evaluate the impact of primary and secondary metasomatic processes on the geochemical systematics of the peridotites..

6.1 Identification of primary and secondary processes

6.1.1 Major element perspective

The mantle peridotites sampled from the Parry Peninsula are all spinel facies, harzburgites or clinopyroxene-poor lherzolites, and are characterized by their fresh mineralogy that permits both olivine separates and whole rock chemical and isotopic analyses. Key aspects of their mineral and whole rock chemistry, e.g., high Fo = 91.9 to 92.6, high spinel Cr# = 32 to 60 – extending to much higher values in the till spinels, low Al_2O_3 contents in both xenolith and concentrate clinopyroxene, low bulk Al_2O_3 (0.45 to 1.2 wt. %) and CaO (0.21 to 0.98 wt. %; **Tables 1, S1a, S4**) are chemical signatures typical of Archean cratonic peridotites (**Figs. 2, 3, 6**). Collectively, these chemical signatures are thought to primarily reflect original high degrees of melt depletion (>28 % to 45 % estimated from Fo contents extrapolated to the 3 GPa and 7 GPa melting curves of Pearson and Wittig, 2008), with minor influence of secondary metasomatic processes (Pearson and Wittig, 2014 and references therein).

Despite the altered nature of the Central Victoria Island peridotites, enough compositional information can be gathered to constrain their origin, once secondary effects have been accounted for. Several peridotites show elevated Al_2O_3 and/or CaO contents that reflect the results of secondary overprinting (**Fig. 6**). The high CaO contents (CaO >3 wt. %; Ca/Al>1.6; high Sr concentrations of > 200 ppm) of the five peridotites (SnO-12, SnO-15, Sno-21, SnO-24 and SnO-29) were likely caused by carbonatitic metasomatism (referred to as carbonation). The two CVI peridotites (SnO-19 and SnO-20) with elevated Al_2O_3 contents (3.6 and 4.6 wt. %; **Fig. 6**; **Table 1**) are accompanied by garnet with the lowest Cr_2O_3 and CaO contents (**Table S1b**). These samples may have experienced significant silicate melt refertilization and recrystallization.

For the remaining CVI peridotites whose major element compositions do not appear significantly affected by carbonation or melt metasomatism, the whole rock and available mineral chemistry, i.e., high olivine Fo 91.7 to 92.4, high spinel Cr# (44 and 81, and higher values in the till spinel), clinopyroxene with low Al_2O_3 contents, and low bulk xenolith Al_2O_3 (0.70-2.20 wt. %) and CaO (0.31-1.61 wt. %) contents (**Tables 1, S1b, S2, S3, S4**), are similar to Archean cratonic peridotites that formed from high degrees (>25 % to 40 % estimated from Fo contents extrapolated to the 3 GPa and 7 GPa melting curves of Pearson and Wittig, 2008) of primary melt depletion (**Figs. 2, 3, 6**). Hence at both localities sampled in northern Canada, major element bulk and mineral compositions of the majority of peridotites reflect primary high degrees of partial melting akin to typical Archean cratonic peridotites.

6.1.2 Garnet trace element perspective

Since nearly all PP peridotites are garnet-free, we focus on the xenolith and till samples from the CVI peridotites. Garnets of the two aluminum-enriched samples (SnO-19 and SnO-20) are characterized by high HREE and Y, and have Type 1 REE patterns (low La/Yb), akin to garnet equilibrated with silicate melt (**Fig. 4A**; **Tables S1b, S3**). Such characteristics are very common among the CVI till garnet (**Fig. 4B**). This type of 'metasomatism' can be inferred to be silicate melt refertilization that drastically modifies both major and trace element compositions. This is also consistent with the observation that the two xenoliths, along with a significant portion of till garnet plot far outside of the 'depleted peridotitic garnet' field defined by Griffin et al. (1999), towards the 'undepleted peridotitic garnet' field in the Zr versus Y diagram (**Fig. 5A**). Considering their suprachondritic Zr/Hf and Ti/Eu ratios (**Fig. 5B**), the metasomatic melt is unlikely to be kimberlite (Shu and Brey, 2015), but instead is more Ti and Al-rich.

Garnets from the remaining CVI xenoliths have complex, sinusoidal REE patterns (**Fig. 4A**) that are also seen in the till garnet population (**Fig. 4C**), and are not compatible with single-stage melt depletion. Such REE patterns are common in cratonic peridotitic garnet and can be interpreted to reflect variable carbonatitic/basaltic melt/fluid metasomatism that modified the trace element compositions but left major element compositions relatively unaffected (Shu and Brey, 2015 and references therein). However, most of these garnets plot within or close to the 'depleted peridotitic garnet' field in the Y versus Zr diagram (**Fig. 5A;** except for sample SnO-12 that shows significant enrichment of both Zr and Y), suggesting their signatures were established by minimal silicate melt metasomatism. More information is revealed by the Zr/Hf versus Ti/Eu systematics of these garnets (Yaxley et al., 1991; Sweeney et al., 1992; Rudnick et al., 1993; Girnis et al., 2013; Shu and Brey, 2015). None of the CVI garnets strictly reside in the depleted mantle region of the Zr/Hf versus Ti/Eu plot (**Fig. 5B**). The garnets of the five carbonated peridotites (including sample SnO-12; CaO >3 wt. %; Ca/Al >1.6; bulk Sr >200ppm), are characterized by suprachondritic Zr/Hf and subchondritic Ti/Eu, consistent with carbonatitic metasomatism (**Fig. 5B**). This is also consistent with their sinusoidal REE patterns that require interaction with small-volume volatile-rich carbonatitic melts/fluids (e.g., Aulbach et al., 2004b). Moreover, garnets from SnO-28 and SnO-35 (Type 3 patterns) have suprachondritic Zr/Hf and Ti/Eu ratios similar to those of the two aluminum-enriched samples (SnO-19 and SnO-20, Type 1 garnet patterns; **Fig. 5B**), suggesting that peridotites SnO-28 and SnO-35 experienced metasomatism by a similar silicate agent, but to a lesser degree relative to the two aluminum-enriched peridotites; the discrepancy in their garnet patterns may reflect their different depths in the mantle column through percolation of the same metasomatic melts. The garnets of the other CVI samples plot within the field of carbonatitic metasomatism or between the field of

carbonatitic metasomatism and silicate melt metasomatism (similar to the kimberlitic melt metasomatism; **Fig. 5B**), including the Type 4 garnet samples (SnO-33 and SnO-34) that have intermediate patterns in between Type 1 and Type 3 patterns (Fig. 4A). Sample SnO-12 (Type 3 garnet pattern) may have been influenced by both carbonatitic and silicate metasomatism in order to account for its chemical diversity, as discussed above (**Figs. 5, 6**). Similar metasomatic histories are evident from garnets from the CVI till. Overall, in combination with bulk and mineral major elements, the garnet trace elements document multiple types of metasomatism/refertilization that influenced the CVI peridotites.

6.1.3. HSE, Se and Te perspective

Unlike lithophile elements in mantle peridotites, HSE, Se and Te are controlled by trace phases, such as base metal sulfides (BMS: Fe-Ni-Cu sulfides) and platinum group minerals (PGM), rather than modally-major phases (e.g., Lorand et al., 2008, 2010; Lorand and Luguet, 2016 and references therein). During mantle partial melting, incongruent melting of BMS produces a Cu-Ni-rich sulfide melt, which is extracted from the silicate melt and concentrates Pt, Pd, Se and Te; at the same time, a monosulfide solid solution (mss) is retained in the peridotitic residue with increasing partial melting, sequestering Os, Ir and Ru (Alard et al., 2000; Luguet et al., 2003; 2007; Bockrath et al., 2004; Ballhaus et al., 2006; Helmy et al., 2010; Brenan, 2015). With increasing partial melting and the subsequent volume decrease of the BMS, PGM such as Pt-Ir-Os, Os-Ru high-temperature sulfides and Os-Ru±Ir alloys will be stabilized in the mantle residue (Luguet et al., 2007; Lorand et al., 2010; 2013; Fonseca et al., 2012). In addition, Re behaves more incompatibly than Pd during mantle partial melting (e.g., Pearson et al., 2004; Luguet et al., 2007). Thus, mantle melt depletion leads to the overall depletion of Re, platinum-

group PGE (PPGE: Pt and Pd), Se and Te relative to Ir-group PGE (IPGE: Os and Ir) (e.g., Lorand and Luguet, 2016 and references therein) in depleted mantle peridotites.

In addition to recording the signature of primary partial melting, mantle peridotites can also experience the percolative infiltration of carbonatitic/silicate melts or fluids postdating partial melting, as clearly recorded by garnets in the mantle peridotites of this study. The 5 distinct HSE patterns groups (Groups A to E) along with the Se-Te systematics observed among the PP and the CVI peridotites are a function of the various melt-rock or fluid-rock reactions that add metasomatic BMS and PGM (e.g., Pt-tellurides) (Lorand et al., 2003a, b; Luguet et al., 2003, 2004; Reisberg et al., 2004; Alard et al., 2002, 2011; Ackerman et al., 2009, 2013; van Acken et al., 2010a,b; Marchesi et al., 2014; Luguet et al., 2015; Lorand and Luguet, 2016; Luguet and Reisberg, 2016) or remove BMS of both residual and metasomatic origin (Lorand et al., 2003a, b, 2004; Reisberg et al., 2004; Ackerman et al., 2009, 2013; Marchesi et al., 2014; Lorand and Luguet, 2016; Luguet and Reisberg, 2016). Collectively, fractionation of HSE along with Se and Te can be used to determine the expected signature of primary melt depletion and evaluate the impact on the HSE-Se-Te systematics plus Re-Os isotopic systematics of metasomatic processes (e.g., Luguet et al., 2015; Lorand and Luguet, 2016; Luguet and Reisberg, 2016 and references therein).

The Group A, Group C and Group D HSE patterns of the CVI peridotites are similar to the three HSE groups (Group 1, 2 and 3) reported for the Letlhakane cratonic peridotites from the southwestern margin of the Zimbabwe craton (Luguet et al., 2015). For the Letlhakane peridotites, Group 1 spinel peridotites are characterized by the most refractory composition (e.g., low CaO (0.42 to 0.85 wt. %) and Al_2O_3 (0.28 to 0.89 wt. %), absence of BMS, extreme depletion of PPGE relative to IPGE (e.g., $Pd_N/Ir_N < 0.07$), and extremely low Se (<14 ppb) and

Te (<1 ppb) abundances that are interpreted to represent the residual peridotites that were least overprinted by metasomatic processes and hence most likely to record the timing of melt depletion. In contrast, the Group 2 and Group 3 peridotites, characterized by less depletion or even enrichment of PPGE relative to IPGE (e.g., Pd_N/Ir_N = 0.1-1.5) and significantly higher Se (15-108 ppb) and Te (1.4-2.8 ppb) abundances, were modelled well by variable (0.001-0.05 % of the whole rock) metasomatic BMS ± PGM addition into the Group 1 residual peridotites during melt-rock reaction (Luguet et al., 2015). Using this interpretative framework, the CVI Group A peridotites (SnO-27 and SnO-32 characterized by extremely low Pd_N/Ir_N of 0.02-0.04) are most likely to represent the residual mantle that suffered minimal metasomatic overprinting, which is consistent with their low CaO (0.31 to 0.62 wt. %) and Al_2O_3 (0.91 to 1.1 wt. %, slightly higher than those of Letlhakane Group 1 spinel peridotites due to the presence of garnet in Group A peridotites) and the lowest garnet MREE-HREE, Y, Zr and Ti concentrations in SnO-32 (trace elements not measured for SnO-27). By contrast, the CVI peridotite Group C (SnO-15, Sn-24 and SnO-33) and Group D (SnO-17, SnO-19, SnO-20, SnO-28, SnO-29, SnO-34 and SnO-35) would represent the increasing addition of metasomatic BMS ± PGM during the percolation of small volumes of silicate melts.

In general, metasomatic processes expressed as enrichment in incompatible lithophile elements in cratonic peridotites do not correlate with their HSE, Se and Te systematics, because HSE, Se and Te elements are controlled by very different host phases when compared to lithophile elements (Lorand et al., 2008, 2010 and references therein). The three Group C CVI peridotites defined by HSE signatures (e.g., intermediate Pd_N/Ir_N = 0.13-0.30; **Fig. 6**), have distinct lithophile element characteristics (e.g., CaO content, garnet trace element patterns; **Figs. 4A, 5**), reflecting different types of metasomatism. A similar scenario occurs in the Group D

peridotites where multiple melt percolation events with different compositions (carbonatitic, kimberlitic, or basaltic; **Fig. 5**) could have taken place. In this group, peridotites SnO-19 and SnO-20 clearly suffered melt refertilization, including the presence of phlogopite, which significantly modified both their lithophile and HSE, Se and Te element compositions resulting from BMS ± PGM addition. In contrast, the other five peridotites in this group (SnO-17, SnO-28, SnO-29, SnO-34 and SnO-35) that share similar HSE-Se-Te signatures have different and very variable lithophile element systematics in garnet. The Group B CVI peridotites (SnO-12 and SnO-21) have Pd and Re characteristics in HSE patterns intermediate between Group A and Group C peridotites, while they have similar lithophile element characteristics (e.g., elevated bulk CaO contents, Type 3 garnet pattern; **Fig. 4A**) resulting from both basaltic and carbonatitic melt metasomatism. Such metasomatic processes in Group B peridotites probably proceeded with precipitation of less BMS than in Group C peridotites.

One group of CVI peridotites is distinct from the others. The Group E peridotites (SnO-26 and SnO-36) are characterized by HSE contents typically lower than the PUM estimates, low Se (below detection limit) and Te (below detection limit to 3.8 ppb) contents and prominent Os depletion relative to Ir (Os_N/Ir_N = 0.18-0.50). Similar strong Os/Ir fractionations have been observed in peridotites elsewhere e.g., Sidamo, East Africa Rift (Lorand et al., 2003), Kerguelen Island, South India Ocean (Lorand et al., 2004), Yangyuan, China (Liu et al., 2010, 2011) and Rio Grande (Harvey et al. 2015). Such HSE characteristics can be potentially explained by the removal/dissolution of sulfide (both residual and, if any, earlier metasomatic sulfide) during the percolation of large volumes of S-undersaturated silicate melt (see Lorand Luguet and Reisberg, 2016) and/or oxidizing melt/fluid that can destabilize BMS (Liu et al., 2010; Aulbach et al., 2016).

The PP peridotites can also be classified within the geochemical framework established for the CVI peridotites. Although the lithophile element data do not show strong metasomatic alteration for the PP peridotites, these rocks and olivine separates are characterized by low, variable HSE abundances, and low Se (below detection limit) and Te (0.35-2.1 ppb) contents in comparison to the CVI peridotites. For approximately half of the PP peridotites, their HSE characteristics are equivalent to the Group E CVI peridotites, while the remaining half fall into the Group A or Group C patterns. Following the criteria applied to the CVI peridotites, it is likely that, other than limited metasomatic BMS± PGM addition in some PP peridotites, the other PP peridotites most likely experienced removal/dissolution of BMS during melt-rock reaction, consistent with the scarcity of BMS in these rocks. Collectively, subsequent to the primary melt depletion, metasomatic overprinting processes have affected to various extents the chemical systematics of the CVI and PP peridotites.

6.2 Influence on Re-Os system and estimating the formation age of lithospheric mantle

6.2.1 Influence of metasomatic processes on Re-Os isotope system

As discussed above, multiple metasomatic processes appear to have modified the lithophile and HSE, Se and Te systematics of the CVI and PP peridotites. Here we try to evaluate the potential effects of these disturbances on the Re-Os isotope system. Both Os and Re show highly siderophile characteristics during planetary differentiation, while they are chalcophile and highly siderophile elements within mantle lithologies and petrological processes affecting the lithospheric mantle. However, during these mantle processes, Re can behave incompatibly given that it has lithophile affinity while Os is compatible during mantle melting (e.g., Fonseca et al., 2007; Luguet et al., 2007; Mallmann and O'Neill, 2007; Brenan, 2008). However, Re does not

closely link with lithophile (e.g., Al_2O_3 content) or other highly siderophile elements (e.g., Pd_N/Ir_N ratio) in the peridotites from Parry Peninsula and Central Victoria Island, because of its partial lithophile character, and the radiogenic ingrowth influence of Re modification on Os isotopic composition will be discussed below. Here we focus on the impact of the different melt rock percolation events (high or low melt-rock ratio, different melt composition) on the Os isotopic compositions using HSE, Se and Te element signatures. One key issue is to examine whether these peridotites were formed by metasomatism of Archean depleted lithospheric mantle.

In fact, the Pd_N/Ir_N ratio which is a key ratio in discerning metasomatic processes, especially those involving addition of metasomatic BMS (Rehkämper et al., 1997; Luguet et al., 2001, 2003, 2015; Pearson et al., 2002; van Acken et al., 2010a; Liu et al., 2010, 2011; Luguet and Reisberg, 2016 and references therein), can be thus used to discuss the robustness of the $^{187}Os/^{188}Os$ ratios and interpret the Re-Os model ages (see Luguet et al., 2015). The CVI Group A, B, C & E peridotites show variable but relatively low Pd_N/Ir_N ratios (0.02-0.36) resulting from partial melting followed by either low degrees of metasomatic addition of BMS ± PGM during melt-rock reaction involving small volumes of silicate melts, or removal/dissolution of BMS during large volumes of melt-rock reaction (e.g., Luguet et al., 2015) or during the percolation of oxidizing melts (Liu et al., 2010; Aulbach et al., 2016). Such metasomatic overprintings on the HSE systematics (e.g., Pd_N/Ir_N, 1/Os and Os_N/Ir_N; **Fig. 9**) of peridotites would have been accompanied by changes in their $^{187}Re/^{188}Os$ ratios (e.g., Luguet and Reisberg, 2016 and references therein). This is evident in the CVI and PP peridotites by the large range of $^{187}Re/^{188}Os$ values obtained and that span from strongly subchondritic to chondritic ratios (**Fig. 10A**). Considering that Pd and Re are incompatible and Os and Ir compatible during mantle

partial melting (Pearson et al., 2004), a highly depleted peridotite will have extremely low Pd/Ir and Re/Os ratios and a high Os concentration (PUM-like to above PUM, see Luguet et al., 2015) in comparison to the extremely low Pd and Re concentrations, as well as low CaO and Al_2O_3 contents. The CVI Group A peridotite SnO-27 has a Pd_N/Ir_N of 0.02, $^{187}Re/^{188}Os$ of 0.022, Os of 7.31 ppb, Re of 0.033 and Pd of 0.13 ppb, which, along with its low CaO (0.31 wt. %) and Al_2O_3 (0.91 wt. %), exactly match these depleted characteristics, and therefore its low Pd/Ir and Re/Os ratios appear to hold a HSE systematics the closest to a peridotitic residue of high partial melting degree. As such, its $^{187}Os/^{188}Os$ ratio is hence likely to be reflecting that of partial melting event. Its T_{RD} age of ~ 2.0 Ga is close to the timing of melt depletion that occurred during lithospheric mantle formation beneath the Central Victoria Island.

However, a residue with such low Re and Pd can be easily modified by addition of small amounts of metasomatic BMS that tend to be Pd-rich and Re-rich (e.g., Alard et al., 2002, 2011). In contrast, addition of minor amounts of metasomatic BMS, although they are also Os-rich, would not affect the whole-rock peridotite Os concentrations, and the shift in the $^{187}Os/^{188}Os$ will primarily be generated by radiogenic ^{187}Os ingrowth of ^{187}Re decay after the metasomatism event took place (e.g., see modelling Figure 11B of Luguet et al., 2015). Likewise, dissolution or removal of BMS during metasomatic events will also modify the Re/Os ratios of the peridotites (e.g., Liu et al., 2010; Luguet et al., 2015; Aulbach et al., 2016). For the CVI Groups A, B, C and E peridotites, no significant variations of $^{187}Os/^{188}Os$ ratios (0.1136-0.1162, one sample having 0.1109; **Fig. 9A**) are observed over a large range of Pd_N/Ir_N (**Fig. 9D**), 1/Os (**Fig. 9E**) or Os_N/Ir_N (**Fig. 9F**), and they plot along or close to the 0.27 Ga (eruption age) reference isochron in the Re-Os isochron diagram (**Fig. 10A**). Our data demonstrate decoupling between indices that trace metasomatic processes experienced by these peridotites and their $^{187}Os/^{188}Os$ ratios. This finding

shows that $^{187}Os/^{188}Os$ was not significantly modified either via limited radiogenic Os addition of BMS or limited radiogenic ^{187}Os ingrowth of ^{187}Re decay due to change of Re/Os ratios. These features may suggest that the major metasomatic processes experienced at least by the CVI peridotites in changing their Re-Os isotope and HSE systematics occurred recently, most likely during or shortly before the kimberlite eruption, or perhaps during the 723 Ma Franklin LIP event. In addition, our data indicate that these CVI peridotites were not formed by metasomatism of Archean depleted lithospheric mantle that would likely retain the Archean peak modes in Re-depletion Os model ages as observed in the typical cratonic peridotites (e.g., Slave, Kaapvaal, North Atlantic cratons; Pearson and Wittig, 2014).

Given the ubiquity of reworking of Archean crust and underlying lithospheric mantle (e.g., Hawkesworth et al., 2017), we consider another possibility that the dominant Os isotopic compositions (i.e., $^{187}Os/^{188}Os$ ~ 0.113 – 0.116) in the CVI Groups A, B, C and E peridotites resulted from mixing of Archean precursor peridotites and younger mantle materials (e.g., from Mackenzie or Franklin plume, or asthenosphere at the time of proto-kimberlite activities). Since Os and other HSE are commonly hosted by BMS and PGM, the homogenization and redistribution of Os isotopic composition would be accompanied by the uniformity of HSE patterns that differ from the variable HSE patterns observed in these rocks (e.g., ranging from low to high Pd_N/Ir_N ratios; **Fig. 7A**). On the contrary, mantle mixing would predict a large range of $^{187}Os/^{188}Os$ ratios in the residual mantle peridotites, for example, as seen in the New Zealand lithospheric mantle (McCoy-West et al., 2013; Liu et al., 2015). We conclude that mixing of Archean precursor peridotite with younger mantle materials is not the process to account for the dominant Os isotopic compositions of these CVI peridotites. Collectively, the Os isotopic compositions of these Groups of CVI peridotites are best interpreted to reflect the signature of

primary melt depletion and therefore are suitable to determine the formation age and stabilization of the lithosphere.

Similarly, the PP peridotites with the HSE systematics similar to Groups A, B, C and E of the CVI peridotites have an almost identical range of $^{187}Os/^{188}Os$ ratios (0.1137-0.1162, one sample having 0.1119; **Fig. 9A**), and overall similar HSE patterns (**Fig. 7**) and elemental characters (**Fig. 9**). Given the scarcity of BMS in the PP peridotites, their HSE are expected to reside in un-identified PGM. Homogenization and redistribution of PGM by mantle mixing under lithosphere conditions would be difficult, as they are predicted to survive in the convective mantle (e.g., Meibom et al., 2002; Alard et al., 2005). Thus, similar to the CVI peridotites, the narrow range of $^{187}Os/^{188}Os$ ratios of the PP peridotites most likely are not a result of mixing of Archean precursor mantle and younger mantle materials. Moreover, the PP whole rock peridotites plot along the 0.27 Ga reference isochron (**Fig. 10A**). Hence they too suffered minor recent metasomatism that did not significantly change their $^{187}Os/^{188}Os$ ratios and are thus likely to yield T_{RD} model ages that are close to the melt depletion event that stabilized the lithospheric mantle in this region. Some of the olivine separates from the PP peridotites have higher $^{187}Re/^{188}Os$ ratios, up to 0.27, which have been observed in olivines from residual peridotites elsewhere (e.g., Hart and Ravizza, 1996; Burton et al., 1999, 2002; Harvey et al., 2010, 2011). Nonetheless, the olivine separates of the PP peridotites plot along the 2 Ga reference isochron (**Fig. 10A**) and thus their Re-Os isotopic systematics have remained intact since formation marking a ~2 Ga formation age, in contrast to the PP whole rock peridotites that lie along the 0.27 Ga reference isochron (**Fig. 10A**).

In contrast to the other peridotites groups, the CVI Group D peridotites are characterized by significantly higher Pd_N/Ir_N ratios (0.69-1.34) that resulted from greater addition of

metasomatic BMS ± PGM than the PP and other CVI peridotites. The clearly defined positive correlation between Pd_N/Ir_N and $^{187}Os/^{188}Os$ in the Group D peridotites (**Fig. 9D**) has two potential explanations: 1) recent metasomatic addition of BMS with highly radiogenic $^{187}Os/^{188}Os$; 2) ancient metasomatic addition of BMS (e.g., as early as a few hundreds of Myrs after the formation of cratonic peridotites; Wainwright et al., 2015; Bragagni et al., 2017; van der Meer et al., 2017). If recent metasomatic addition of BMS into the ancient depleted peridotites was to account for the observed variable $^{187}Os/^{188}Os$, it requires the introduction of fairly large amounts of radiogenic ^{187}Os. This would lead to a negative correlation between $^{187}Os/^{188}Os$ and 1/Os (or even $^{187}Re/^{188}Os$), which is not observed (**Fig. 9E; Fig. 10**). When considering more ancient metasomatism of the Group D peridotites, we might expect an isochron correlation if all the starting peridotites were of the same age and highly depleted, with restricted Os isotope compositions due to their low Re contents. Although there is a scattered Re-Os "isochron" correlation for the Group D peridotites, its slope gives an age of 3.8 Ga that is significantly older than any model age calculated from the initial $^{187}Os/^{188}Os$ (**Fig. 10A**), and no crustal rocks of this age are known in the vicinity. Furthermore, this steep correlation in Re-Os isotope space intersects, at its lower end, the main cluster of CVI and PP peridotites that give ~ 2 Ga model depletion ages, making an age of metasomatism in the Eoarchean highly unlikely. Also, to add complexity to the Group D story, despite their large range of Pd_N/Ir_N, extending to suprachondritic ratios, they have very low to low $^{187}Re/^{188}Os$ ratios (0.008-0.18, one up to 0.45), on average lower than those of the other CVI peridotites (0.022-0.31). This observation seems to imply recent Re loss relative to Os in the Group D peridotites. Thus, the CVI Group D peridotites may have experienced ancient metasomatic addition of BMS, possibly during the massive Mackenzie LIP event at circa 1.3 Ga (LeCheminant and Heaman, 1989) but suffered

recent Re loss relative to Os, lowering the Re/Os ratios probably due to the volatility or mobility of Re (e.g., Borisov and Jones, 1999; Xiong and Wood, 1999; Becker et al., 2001; Lassiter, 2003; Sun et al., 2003; Yudovskaya et al., 2008; Dale et al., 2009; Coggon et al., 2015), most likely during kimberlite ascent or eruption.

The mineralogical controls on the contrasting Re behavior between the CVI Group D and other peridotite Groups remain unclear and deserve further investigation. The Group D peridotites that suffered significant secondary modification of Os isotopic compositions are thus not suitable for determination of the formation age and stabilization of the lithosphere using Os model ages. Exceptionally, within the CVI Group D peridotites, peridotite SnO-11 has the highest Os concentration (16.3 ppb) rendering its Os isotopic systematics more robust to metasomatism, consistent with its lowest $^{187}Re/^{188}Os$ (0.008) and $^{187}Os/^{188}Os$ (0.1144) in the group (**Fig. 9**, **Fig. 10A**). This Group D peridotite gives a T_{RD} model age that is completely in line with the ~ 2 Ga model ages of the other peridotite groups. Apart from nugget effects that cause heterogeneity of HSE in mantle peridotites, another interpretation for such high Os concentrations and low $^{187}Os/^{188}Os$ in these rocks is via precipitation of Os along with other IPGE (Ir, Ru) from depleted peridotites with low $^{187}Os/^{188}Os$ (e.g., the other groups of CVI peridotites) through percolation of a S-undersaturated melt (Ackerman et al., 2009). However, HSE saturation (i.e., forming alloys) in silicate melts is very unlikely to occur before the S saturation (Lorand et al., 2003 a, b; Luguet et al., 2003; Luguet and Reisberg, 2016). This is supported by the data of peridotite SnO-11 characterized by both high IPGE and PPGE abundances, requiring addition of metasomatic BMS that may not have come from the PPGE-depleted peridotites. Thus, multiple processes most likely occurred to account for the HSE and Os isotopic compositions in peridotites like SnO-11. Also, within group D, peridotite SnO-34 has

a high $^{187}Re/^{188}Os$ (0.18) and a low $^{187}Os/^{188}Os$ (0.1148), plotting along the 0.27 Ga reference isochron (**Fig. 10A**), which may suggest that this peridotite experienced recent metasomatism, instead of ancient metasomatism. Hence, even within the clearly disturbed Group D peridotite class, there are peridotites whose Os model ages may approximate the time of melt depletion and lithosphere depletion.

6.2.2 Osmium model ages and the formation age of lithospheric mantle

Despite the absence of correlations between Re and lithophile (e.g., Al_2O_3 content) or other HSE (e.g., Pd/Ir ratio), Se and Te of the peridotites from Parry Peninsula and Central Victoria Island, Re abundance in residual mantle could be easily affected by kimberlitic contamination that raises Re abundances over Os (e.g., Rao et al., 2013; Tappe et al., 2017). This is supported by the observation that most peridotites plot closely along the 0.27 Ga reference isochron in the Re-Os isochron diagram (**Fig. 10A**), except for the 5 CVI Group D samples (SnO-17, SnO-28, SnO-29, SnO-34 and SnO-35) that likely experienced ancient metasomatism and are not considered here in constraining the formation age and stabilization of the lithosphere beneath Arctic Canada. Therefore, part of the Re introduction into the CVI and PP peridotites occurred recently, most likely associated with, or shortly before, kimberlite eruption (e.g., Irvine et al., 2001; Pearson et al., 2004; Liu et al., 2016). Consequently, in determining the melt depletion ages of the mantle peridotites using Re-Os model ages, all the measured Re can be assumed to be derived from kimberlite infiltration during eruption, and the radiogenic ingrowth of ^{187}Os from ^{187}Re decay since eruption time should be corrected for to deduce the initial $^{187}Os/^{188}Os$ ratios used to calculate their rhenium-depletion model ages ($T_{RDeruption}$; **Fig. 10B**; Walker et al., 1989; Pearson et al., 1995). It should always be noted that the resulting $T_{RDeruption}$

ages are still minimal estimates for the melt depletion ages of the peridotites, considering that it is possible that at least part of Re could be added into the rock well before the kimberlite infiltration or was left after partial melting.

Using the $T_{RDeruption}$ model age approach, the Parry Peninsula bulk rocks define a clear mode in model age at 2.0 ± 0.2 Ga (**Fig. 11A**), consistent with the 2 Ga isochron age of their olivine separates (**Fig. 10A**), although olivine separates have slightly more variable $T_{RDeruption}$ ages (**Fig. 11A**). These ages (~2 Ga) are significantly younger than the main $T_{RDeruption}$ peak mode of the Archean cratonic peridotites (>2.5 Ga; see review in Pearson and Wittig, 2014).

$T_{RDeruption}$ model ages calculated for the Group A, B, C and E CVI peridotites are remarkably similar ranging between 1.8 and 2.2 Ga with a pronounced mode of ~2 Ga (**Fig. 11B**) identical to that in peridotites from Parry Peninsula (**Fig. 11**A). The exception is a single peridotite, SnO-12, that gives a $T_{RDeruption}$ age around 2.4-2.5 Ga (**Fig. 11**B). This sample may reflect heterogeneity of the Os isotope composition of the convecting mantle from which these peridotites were derived, in the same way that much larger heterogeneity and anomalously old ages are recorded in other peridotites from the oceanic and continental lithosphere (e.g., Alard et al., 2005; Harvey et al., 2006; Pearson et al., 2007; Liu et al., 2008, 2015). It is less likely that metasomatic enrichment of Archean precursor peridotites at two separate localities in northern Canada would produce the same model age peak at each location.

The Re-Os isotope systematics of the least disturbed of the CVI and PP peridotites shows clearly that there is no evidence to support the existence of major blocks of Archean lithospheric mantle beneath the Central Victoria Island, or the Parry Peninsula despite the similarity in bulk compositions of the peridotites to cratonic mantle. This Paleoproterozoic formation age (~2 Ga) for the lithospheric mantle underpinning these regions is distinct from the Neoarchean mode in

model ages evident for Slave craton peridotites (e.g., Heaman and Pearson, 2010). The significance of the Paleoproterozoic age for the lithospheric mantle beneath these two regions of Arctic Canada will be explored below in the context of their diamond potential.

6.3 Lithosphere thickness and mantle sampling beneath the Parry peninsula and Central Victoria Island

Due to the refractory nature of the mantle xenoliths erupted from beneath the Parry Peninsula, and the altered state of the CVI peridotites, orthopyroxene is very scarce. As such we employ the Nimis and Taylor (2000) single clinopyroxene thermobarometer (using the screens recommended by Grütter (2009)), on pyroxene derived from coarse concentrate from local till sampling (**Table S6**). Paleogeotherms were fitted to the resulting data using the procedure documented in Mather et al. (2011). Temperatures determined from the Ni contents of garnet were extrapolated to the resulting mantle geotherms to give an idea of the depth of mantle sampling of the kimberlites from these two regions (**Table S3**).

Parry Peninsula xenolith clinopyroxene grains (n=10) give temperatures ranging from 621 to 839 ºC and pressures from 2.2 to 3.1 GPa (**Table S6**a), whereas the clinopyroxene grains from concentrate (n=352) give higher temperatures (813-1293 ºC) and pressures (3.0-6.2 GPa) reflecting a much more representative sampling of the lithospheric mantle than the xenoliths. The xenolith-derived clinopyroxene data cluster at low P-T and do not allow for an accurate geotherm regression, generating a relatively shallow (and hot) geotherm estimate with large uncertainties (**Fig. S8**). However, clinopyroxene data from concentrate in which high-T mineral grains that do not reflect a conductive geotherm have been screened out were utilized to generate a paleogeotherm with the thickness of the lithosphere beneath the Parry Peninsula as 180 ± 20 km

(**Fig. 12**; **Fig. S8**). This depth range is consistent with the presence of a seismically fast root to at least 150 km depth (Schaeffer and Lebedev, 2014). Furthermore, the lithosphere extends into the diamond stability field (consistent with the observation that these kimberlites are diamond-bearing), but is thinner than that estimated beneath the central Slave craton (~ 230km; e.g., Grütter, 2009). Nonetheless, this lithospheric thickness is within the range of lithospheric mantle depths found beneath cratons globally (e.g., Mather et al., 2011).

Clinopyroxene grains (n=196) recovered from Central Victoria Island mineral concentrate yield an estimate for the thickness of the lithosphere beneath that region of about 215 ± 30 km, identical within error to the thickness of lithosphere beneath the central Slave craton (**Fig. 12**) and consistent with an independent estimate by Kolebaba et al. (2003). The Ni-in-garnet temperature data (**Table S3**) indicates that mantle sampling by the CVI kimberlites took place right through the diamond window indicated by the clinopyroxene geotherm. These estimates, along with the recorded presence of diamonds in both Parry Peninsula (Davies and Davies, 2013) and CVI kimberlites (Kolebaba et al., 2003) clearly indicate the presence of diamond-facies lithospheric mantle (of variable thickness) beneath both the Parry Peninsula and Central Victoria Island.

6.4 Implications and diamond potential of Paleoproterozoic lithosphere

Collectively, the mineral and whole rock chemistry of mantle xenoliths from both the Parry Peninsula and Central Victoria Island regions of Arctic Canada, allow new estimates for the thickness of the lithosphere underpinning these regions that agree with the diamondiferous nature of the kimberlites from both localities. The lithosphere thickness determinations and the highly depleted major element and mineral compositions of their constituent peridotites

notionally indicate the presence of lithospheric mantle roots similar to those beneath typical Archean cratons, such as the central Slave craton, despite the fact that both these regions are far from the clearly defined boundaries of any cratons. However, the modes in Re depletion model ages along with the HSE-Os isotope systematics of the least disturbed peridotites from these regions indicate that this depleted, thick lithospheric mantle formed in the Paleoproterozoic (~2 Ga), rather than the Archean (**Fig. 11**). Hence, while the lithospheric mantle beneath the Parry Peninsula is cratonic in composition, the age constraints, along with the lack of exposed Archean crustal basement do not support the notion of an "Archean MacKenzie craton" as proposed by some diamond explorers (e.g., Davies and Davies, 2013). Similarly, although there is limited evidence for Archean crust in Central Victoria Island (LeCheminant et al., 1996), there is no substantial justification for extending the presence of Slave Craton, in particular its Archean lithospheric mantle northwards and up through this area as proposed on some craton boundary maps (e.g., Bleeker, 2003).

Our Re-Os isotopic signatures on whole-rock peridotites indicate the existence of diamondiferous Paleoproterozoic lithospheric mantle roots beneath two regions of Arctic Canada, with chemical and physical features similar to typical cratonic mantle. This is a clear indication that the Archean is not the only period in Earth history that witnessed the generation of highly depleted melt residues to form craton-like thick refractory lithosphere. Similar suggestions have been made for part of the lithospheric mantle beneath Udachnaya and Obnazhennaya, Siberian craton, based on a preponderance of 2 Ga peridotite model ages (Ionov et al., 2015a,b).

An important question in the light of our results is, how was such diamondiferous Paleoproterozoic lithospheric mantle formed? The relatively low precision of the mantle Os

isotopic evolution curve, at circa ±0.2 Ga (Rudnick and Walker, 2009) means that linking the formation of lithospheric mantle to regional tectonic events in the Northwest Territories and Nunavut is problematic to quantify. Nonetheless, there are a number of major regional tectono-magmatic events that span the age mode defined by the Parry Peninsula and Central Victoria Island peridotites. The age modes of the peridotites from both localities broadly overlap the 2.4 to 2.1 Ga crustal Nd model ages in the Wopmay orogeny (Bowring and Podosk, 1989), as well as the events of the main Wopmay orogeny (1.91-1.71 Ga), collision of the Hottah arc terrains (~1.91 Ga) and subsequent Great Bear arc evolution (1.88-1.86 Ga; Hoffman, 1989; Ootes et al., 2015) (**Fig. 1**). All of these events are related to lateral accretion and the generation of basaltic-andesitic rocks (e.g., Ootes et al., 2015). We speculate that the highly depleted bulk rock compositions were developed during mantle melting associated with hydrous metasomatism in individual or numerous Paleoproterozoic arc systems, as has been suggested for some Archean lithosphere (e.g., Simon et al., 2007; Pearson and Wittig, 2008), followed by subsequent accretion along the margin of the Slave craton to form a craton-like thick lithosphere with significant diamond potential. Identifying corresponding melts produced from the high degrees of melting is, however, problematic due to the overall paucity of exposed ultramafic magmatic rocks.

While it has been widely accepted that there are thermal differences between cratonic and circum-cratonic lithosphere in the Kaapvaal craton and surrounding mobile belts (MacGregor, 1975; Boyd and Gurney, 1986), more recent work has shown that in fact the paleogeotherms derived from mantle xenoliths erupted through Paleoproterozoic terrains at the time of kimberlite eruption were broadly similar within the interior of the craton and around the margin of the craton (e.g., Boyd et al., 2004; Janney et al., 2010; Mather et al., 2011). The main difference in

the xenolith-derived paleogeotherms in southern Africa seems to be recent evidence for thinning associated with a localized basal thermal disturbance that did not have time to re-equilibrate the shallower portions of the mantle geotherm.

The cool mantle paleogeotherms defined by the mantle xenoliths studied here, underpinning Paleoproterozoic crust of the Wopmay orogen resolve an issue raised by Hasterock and Chapman (2011) related to the study of crustal heat flow. These authors identified higher crustal heat flow in the region affected by the Wopmay orogeny, which they suggested is balanced by high crustal heat generation, and speculated that the mantle beneath the Wopmay terrane is probably more consistent with a cratonic geotherm. This is confirmed by our mantle xenolith study. This cool craton-like paleogeotherm had clearly relaxed from any potential thermal disturbance associated with the 1.27 Ga MacKenzie or 723 Ma Franklin events, consistent with a thermal time-constant for thick lithospheric mantle of only two to three hundred Myr (Jaupart and Marechal, 2011). This low level of disturbance is consistent with the absence of MacKenzie and Franklin ages in the Os isotope signatures (**Fig. 11**B). The presence of a diamondiferous mantle root generated in the Paleoproterozoic Era points to diamond generation in mantle roots stabilized after the Archean.

7. Conclusions

The chemical composition of peridotites and mineral concentrate from both the Parry Peninsula and Central Victoria Island is indistinguishable from that of typical Archean cratonic mantle lithosphere. The cool mantle paleogeotherms defined by these peridotites/mineral concentrate reveal that the lithospheric mantle beneath both areas extended well into the diamond stability field at the time of kimberlite eruption, consistent with the recovery of

diamonds from both kimberlite fields. Bulk xenolith HSE-Se-Te abundance and Re-Os isotope data suggest that the mantle beneath these parts of Arctic Canada formed in the Paleoproterozoic Era, at ~2 Ga, rather than in the Archean. Thus, the presence of a diamondiferous Paleoproterozoic mantle root is part of the growing body of evidence across the globe for diamond generation in mantle roots that stabilized well after the Archean. The post-Archean arc terrane accreted along the margin of an Archean craton has formed a craton-like thick lithosphere with significant diamond potential. This serves to demonstrate the importance of subduction accretion in building up Earth's continental masses.

Acknowledgements

This research was supported by funding from the Canada Excellence Research Chairs program to DGP and China "1000 Youth Talents Program" to JL. We are grateful to Diamonds North Resources, Darnley Bay Resources, DeBeers Canada (in particular Mike Seller), the Geological Survey of Canada and the Northwest Territories Geological Survey for supporting sample collection and/or data share. We thank Andrew Locock for providing assistance in the EMPA analyses, Garrett Harris, Sarah Woodland and Chiranjeeb Sarkar for help in the lab, Kathy Mather for discussion on the FITPLOT method, and Yong Xu for drafting the geologic map. We also thank Sonja Aulbach, Lucas Ackerman and one anonymous reviewer for their constructive comments that improved the quality of this manuscript and Associate Editor Rich Walker for his efficient editorial handling. This is publication no. 53 of the ICP-MS and Laser Facility, Steinmann Institute, University of Bonn, and petrogeochemical contribution no. PGC2015-0031 (RIG-no.1) of China University of Geosciences (Beijing).

References

Ackerman L., Walker R. J., Puchtel I. S., Pitcher L., Jelinek E. and Strnad L., 2009. Effects of melt percolation on highly siderophile elements and Os isotopes in subcontinental lithospheric mantle: A study of the upper mantle profile beneath Central Europe. Geochimica et Cosmochimica Acta 73, 2400-2414.

Ackerman, L., Pitcher, L., Strnad, L., Puchtel, I.S., Jelínek, E., Walker, R.J., Rohovec, J., 2013. Highly siderophile element geochemistry of peridotites and pyroxenites from Horní Bory, Bohemian Massif: implications for HSE behaviour in subduction-related upper mantle. Geochimica et Cosmochimica Acta 100, 158–175.

Alard O., Griffin W. L., Lorand J. P., Jackson S. E. and O'Reilly S. Y., 2000. Non-chondritic distribution of the highly siderophile elements in mantle sulphides. Nature 407, 891-894.

Alard, O., Griffin, W.L., Pearson, N.J., Lorand, J.-P., O'Reilly, S.Y., 2002. New insights into the Re–Os systematics of sub-continental lithospheric mantle from in situ analysis of sulphides. Earth and Planetary Science Letters 203, 651-663.

Alard O., Lorand J. P., Reisberg L., Bodinier J. L., Dautria J. M. and O'Reilly S. Y., 2011. Volatile-rich Metasomatism in Montferrier Xenoliths (Southern France.: Implications for the Abundances of Chalcophile and Highly Siderophile Elements in the Subcontinental Mantle. Journal of Petrology 52, 2009-2045.

Arai, S., 1994. Characterization of spinel peridotites by olivine-spinel compositional relationships: review and interpretation. Chemical Geology 113, 191-204.

Aulbach, S., Griffin, W.L., Pearson, N.J., O'Reilly, S.Y., Kivi, K., Doyle, B.J., 2004a. Mantle formation and evolution, Slave Craton: constraints from HSE abundances and Re–Os isotope systematics of sulfide inclusions in mantle xenocrysts. Chemical Geology 208, 61-88.

Aulbach, S., Griffin, W.L., O'Reilly, S.Y., McCandless, T.E., 2004b. Genesis and evolution of the lithospheric mantle beneath the Buffalo Head Terrane, Alberta (Canada). Lithos 77, 413-451.

Aulbach, S., Griffin, W., J. Pearson, N., O'Reilly, S., Doyle, B., 2007. Lithosphere formation in the central Slave Craton (Canada): Plume subcretion or lithosphere accretion? Contributions to Mineralogy and Petrology 154(4), 409-427.

Aulbach, S., Stachel, T., Heaman, L.M., Carlson, J.A., 2011. Microxenoliths from the Slave craton: Archives of diamond formation along fluid conduits. Lithos 126, 419-434.

Aulbach, S., Mungall, J.E., Pearson, D.G., 2016. Distribution and Processing of Highly Siderophile Elements in Cratonic Mantle Lithosphere. Rev Mineral Geochem 81, 239-304.

Ballhaus C., Bockrath C., Wohlgemuth-Ueberwasser C., Laurenz V. and Berndt J., 2006. Fractionation of the noble metals by physical processes. Contributions to Mineralogy and Petrology 152, 667-684.

Becker, H., Shirey, S.B., Carlson, R.W., 2001. Effects of melt percolation on the Re-Os systematics of peridotites from a Paleozoic convergent plate margin. Earth and Planetary Science Letters 188, 107-121.

Becker, H., Horan, M.F., Walker, R.J., Gao, S., Lorand, J.P., Rudnick, R.L., 2006. Highly siderophile element composition of the Earth's primitive upper mantle: Constraints from new data on peridotite massifs and xenoliths. Geochimica et Cosmochimica Acta 70, 4528-4550.

Berman, R.G., Sanborn-Barrie, M., Stern, R.A., Carson, C.J., 2005. Tectonometamorphism at ca. 2.35 and 1.85 Ga in the Rae Domain, western Churchill Province, Nunavut, Canada: insights

from structural, metamorphic and in situ geochronological analysis of the southwestern Committee Bay Belt. Canadian Mineralogist 43, 409-442.

Bernstein, S., Hanghøj, K., Kelemen, P.B., Brooks, C.K., 2006. Ultra-depleted, shallow cratonic mantle beneath West Greenland: dunitic xenoliths from Ubekendt Ejland. Contribution to Mineralogy and Petrology 152, 335-347.

Bernstein, S., Kelemen, P.B., Brooks, C.K., 1998. Depleted spinel harzburgite xenoliths in Tertiary dykes from East Greenland: restites from high degree melting. Earth and Planetary Science Letters 154, 221-235.

Bleeker, W., 2003. The late Archean record: a puzzle in ca. 35 pieces. Lithos 71, 99-134.

Bockrath C., Ballhaus C. and Holzheid A., 2004. Fractionation of the platinum-group elements during mantle melting. Science 305, 1951-1953.

Borisov A., and Jones, J. H., 1999. An evaluation of Re, as an alternative to Pt, for the 1 bar loop technique; an experimental study at 1400 degrees C. American Mineralogist 84, 1528-1534.

Bowring, S.A., and Podosek, F.A., 1989. Nd isotopic evidence from Wopmay Orogen for 2.0-2.4 Ga crust in western North America: Earth and Planetary Science Letters 94, 217-230.

Boyd F. R. and Mertzman S. A., 1987. Composition of structure of the Kaapvaal lithosphere, southern Africa. In: Magmatic Processes - Physicochemical Principles, B.O. Mysen, Ed., The Geochemical Society, Special Publication, 1.

Boyd, F.R., 1989. Compositional distinction between oceanic and cratonic lithosphere. Earth and Planetary Science Letters 96, 15-26.

Boyd, F.R., Gurney, J.J., 1986. Diamonds and the African Lithosphere. Science 232, 472-477.

Boyd, F.R., Pearson, D.G., Hoal, B.G., Nixon, P.H., Kingston, M.J., and Mertzman, S.A., 2004. Garnet lherzolites from Louwrensia, Namibia: bulk composition and P/T relations. Lithos77, 573-592.

Bragagni A., Luguet A., Fonseca R. O. C., Pearson D. G., Lorand J. P., Nowell G. M. and Kjarsgaard B. A., 2017. The geological record of base metal sulfides in the cratonic mantle: A microscale $^{187}Os/^{188}Os$ study of peridotite xenoliths from Somerset Island, Rae Craton (Canada). Geochimica et Cosmochimica Acta 216, 264-285.

Brenan, J.M., 2008. Re–Os fractionation by sulfide melt–silicate melt partitioning: A new spin. Chemical Geology 248, 140-165.

Brenan J. M., 2015. Se-Te fractionation by sulfide-silicate melt partitioning: Implications for the composition of mantle-derived magmas and their melting residues. Earth and Planetary Science Letters 422, 45-57.

Burton K. W., Gannoun A., Birck J. L., Allegre C. J., Schiano P., Clocchiatti R. and Alard O., 2002. The compatibility of rhenium and osmium in natural olivine and their behaviour during mantle melting and basalt genesis. Earth and Planetary Science Letters 198, 63-76.

Burton K. W., Schiano P., Birck J. L. and Allegre C. J., 1999. Osmium isotope disequilibrium between mantle minerals in a spinel-lherzolite. Earth and Planetary Science Letters 172, 311-322.

Campbell, F.H.A., 1981. Stratigraphy and tectono-depositional relationships of the Proterozoic rocks of Hadley Bay, Northern Victoria Island, district of Franklin. Current Research, Volume Paper 81-1A, Geological Survey of Canada, p. 15-22.

Canil, D., 1999. The Ni-in-garnet geothermometer: calibration at natural abundances. Contrib Mineral Petr 136, 240-246.

Carlson, R.W., Pearson, D.G. and James, D.E., 2005. Physical, chemical and chronological characteristics of continental mantle. Reviews of Geophysics 43, 1-24.

Coggon, J.A., Luguet, A., Fonseca, R.O.C., Lorand, J.-P., Heuser, A., Appel, P.W.U., 2015. Understanding Re–Os systematics and model ages in metamorphosed Archean ultramafic rocks: A single mineral to whole-rock investigation. Geochimica et Cosmochimica Acta 167, 205-240.

Dale, C.W., Burton, K.W., Pearson, D.G., Gannoun, A., Alard, O., Argles, T.W., Parkinson, I.J., 2009. Highly siderophile element behaviour accompanying subduction of oceanic crust: Whole rock and mineral-scale insights from a high-pressure terrain. Geochimica et Cosmochimica Acta 73, 1394-1416.

Davies, R., and Davies, A.W., 2013. Zone of Anomalous Mantle, in Pearson, D.G., ed., Proceedings of 10th International Kimberlite Conference, Volume 2, Special Issue of the Journal of the Geological Society of lndia, p.143-156.

Day, H.W., 2012. A revised diamond–graphite transition curve. American Mineralogist 97, 52–62.

Diamonds North press statement (DNR), 2006. DIAMONDS NORTH Shifts Focus on Victoria Island, http://www.marketwired.com/press-release/DIAMONDS-NORTH-Shifts-Focus-on-Victoria-Island-577294.htm.

Fonseca, R.O., Mallmann, G., O'Neill, H.S.C., and Campbell, I.H., 2007. How chalcophile is rhenium? An experimental study of the solubility of Re in sulphide mattes. Earth and Planetary Science Letters 260(3), 537-548.

Girnis, A., Bulatov, V.K., Brey, G.P., Gerdes, A., Höfer, E.H., 2013. Trace element parti-tioning between mantle minerals and silicate–carbonate melts at 6–12GPa and applications to mantle metasomatism and kimberlite genesis. Lithos 160–161, 183–200.

Grégoire, M., Bell, D.R., and Le Roex, A.P., 2003. Garnet lherzolites from the Kaapvaal craton (South Africa): Trace Element evidence for a metasomatic history. Journal of Petrology 44, 629-657.

Griffin, W.L., Doyle, B.J., Ryan, C.G., Pearson, N.J., O'Reilly, S.Y., Davies, R., Kivi, K., Van Achterbergh, E., Natapov, L.M., 1999. Layered mantle lithosphere in the Lac de Gras area, Slave Craton: Composition, structure and origin. Journal of Petrology 40, 705-727.

Grütter, H.S., Gurney, J.J., Menzies, A.H., Winter, F., 2004. An updated classification scheme for mantle-derived garnet, for use by diamond explorers. Lithos 77, 841-857.

Grütter, H., Latti, D., Menzies, A., 2006. Cr-saturation arrays in concentrate garnet compositions from kimberlite and their use in mantle barometry. Journal of Petrology 47, 801-820.

Grütter, H.S., 2009. Pyroxene xenocryst geotherms: Techniques and application. Lithos 112, Supplement 2, 1167-1178.

Gurney, J.J., 1984. A correlation between garnets and diamonds, in Glover, J.E., and Harris, P.G., eds., Kimberlite occurrence and origins: a Basis for Conceptual Models in Exploration: University of Western Australia, Geology Department and University Extension, Publication 8, 143-166.

Gurney, J.J., Helmstaedt, H.H., Richardson, S.H., Shirey, S.B., 2010. Diamonds through time. Economic Geology and the Bulletin of the Society of Economic Geologists 105(3), 689–712.

Hart S. R. and Ravizza G., 1996. Os partitioning between phases in lherzolite and basalt. Isotopic Studies of Crust-mantle Evolution , AGU Monograph, 95, 123-134.

Harte B., 1977. Rock Nomenclature with Particular Relation to Deformation and Recrystallization Textures in Olivine-Bearing Xenoliths. Journal of Geology 85, 279-288.

Harvey J., Dale C. W., Gannoun A. and Burton K. W., 2011. Osmium mass balance in peridotite and the effects of mantle-derived sulphides on basalt petrogenesis. Geochimica et Cosmochimica Acta 75, 5574-5596.

Harvey J., Gannoun A., Burton K. W., Schiano P., Rogers N. W. and Alard O., 2010. Unravelling the effects of melt depletion and secondary infiltration on mantle Re-Os isotopes beneath the French Massif Central. Geochimica et Cosmochimica Acta 74, 293-320.

Harvey, J., Gannoun, A., Burton, K.W., Rogers, N.W., Alard, O., Parkinson, I.J., 2006. Ancient melt extraction from the oceanic upper mantle revealed by Re-Os isotopes in abyssal peridotites from the Mid-Atlantic ridge. Earth and Planetary Science Letters 244, 606-621.

Harvey, J., Konig, S., Luguet, A., 2015. The effects of melt depletion and metasomatism on highly siderophile and strongly chalcophile elements: S-Se-Te-Re-PGE systematics of peridotite xenoliths from Kilbourne Hole, New Mexico. Geochimica et Cosmochimica Acta 166, 210-233.

Hasterok, D., Chapman, D.S., 2011. Heat production and geotherms for the continental lithosphere. Earth and Planetary Science Letters 307, 59-70.

Hawkesworth, C.J., Cawood, P.A., Dhuime, B., Kemp, T.I.S., 2017. Earth's Continental Lithosphere Through Time. Annual Review of Earth and Planetary Sciences 45, 169-198.

Heaman, L.M., Pearson, D.G., 2010. Nature and evolution of the Slave Province subcontinental lithospheric mantle. Canadian Journal of Earth Sciences 47, 369-388.

Heaman, L.M., Kjarsgaard, B.A., and Creaser, R.A., 2003. The timing of kimberlite magmatism in North America: implications for global kimberlite genesis and diamond exploration: Lithos 71, 153-184.

Helmy H. M., Ballhaus C., Wohlgemuth-Ueberwasser C., Fonseca R. O. C. and Laurenz V., 2010. Partitioning of Se, As, Sb, Te and Bi between monosulfide solid solution and sulfide melt - Application to magmatic sulfide deposits. Geochimica et Cosmochimica Acta 74, 6174-6179.

Herrmann, W., and Berry, R.F., 2002. MINSQ-a least squares spreadsheet method for calculating mineral proportions from whole rock major element analysis: Geochemistry: Exploration, Environment, Analysis 2, 361-368.

Hoffman, P.F., 1989. Precambrian geology and tectonic history of North America. The Geology of North America, Volume A, The Geological Society of America, p. 447-512.

Hornal, R.W., Sobczak, L.W., Burke, W.E.F., and Stephens, L.E., 1970. Preliminary results of gravity surveys of the Mackenzie Basin and Beaufort Sea, Gravity map surveys, Earth Physics, Department of Energy, Mines and Resources, Ottawa.

Ionov, D.A., Shirey, S.B., Weis, D., Brügmann, G., 2006. Os–Hf–Sr–Nd isotope and PGE systematics of spinel peridotite xenoliths from Tok, SE Siberian craton: Effects of pervasive metasomatism in shallow refractory mantle. Earth and Planetary Science Letters 241, 47-64.

Ionov, D.A., Doucet, L.S., Carlson, R.W., Golovin, A.V., Korsakov, A.V., 2015a. Post-Archean formation of the lithospheric mantle in the central Siberian craton: Re–Os and PGE study of peridotite xenoliths from the Udachnaya kimberlite. Geochimica et Cosmochimica Acta 165, 466-483.

Ionov, D.A., Carlson, R.W., Doucet, L.S., Golovin, A.V., Oleinikov, O.B., 2015b. The age and history of the lithospheric mantle of the Siberian craton: Re–Os and PGE study of peridotite xenoliths from the Obnazhennaya kimberlite. Earth and Planetary Science Letters 428, 108-119.

Irvine, G.J., Pearson, D.G., and Carlson, R.W., 2001. Lithospheric mantle evolution of the Kaapvaal Craton: A Re-Os isotope study of peridotite xenoliths from Lesotho kimberlites. Geophysical Research Letters 28, 2505-2508.

Irvine, G.J., Pearson, D.G., Kjarsgaard, B.A., Carlson, R.W., Kopylova, M.G., Dreibus, G., 2003. A Re-Os isotope and PGE study of kimberlite-derived peridotite xenoliths from Somerset Island and a comparison to the Slave and Kaapvaal cratons. Lithos 71, 461-488.

Janney, P.E., Shirey, S.B., Carlson, R.W., Pearson, D.G., Bell, D.R., Le Roex, A.P., Ishikawa, A., Nixon, P.H., Boyd, F.R., 2010. Age, Composition and Thermal Characteristics of South African Off-Craton Mantle Lithosphere: Evidence for a Multi-Stage History. J Petrol 51, 1849-1890.

Jaupart, C., and Marechal, J.-C., 2011. Heat Generation and Transport in the Earth. Cambridge, UK, Cambridge University Press, 477 p.

Jaques, A.L., Haggerty, S.E., Lucas, H., Boxer, G.L., 1989. Geochemistry of the Argyle (AK1) lamproite pipe, Western Australia. Kimberlites and Related Rocks, Vol. 1, Their Composition, Occurrence, Origin and Emplacement: In: Ross, J., et al. (Ed.), Geological Society of Australia Special Publication, vol. 14, p. 171–188.

Kennedy, C.S., Kennedy, G.C., 1976. The equilibrium boundary between graphite and diamond. Journal of Geophysical Research 81, 2467–2470.

Kjarsgaard, B.A., 1996. Kimberlite-hosted diamond deposits, Geology of Canadian Mineral Deposit Types, O.R. Eckstrand, W.D. Sinclair, and R.I. Thorpe (ed.); Decade of North American Geology, Geology of Canada, no. 8, p. 557 - 566.

Kolebaba, M., Read, G., Kahlert, B., and Kelsch, D., 2003, Diamondiferous kimberlites on Victoria Island, Canada, a northern extension of the Slave Craton, 8th International Kimberlite Conference, Volume Extended Abstracts: Victoria, Canada, p. 308.

König, S., Lorand, J.P., Luguet, A., Pearson, D.G., 2014. A non-primitive origin of near-chondritic S-Se-Te ratios in mantle peridotites; implications for the Earth's late accretionary history. Earth and Planetary Science Letters 385, 110-121.

Kopylova, M.G., Russell, J.K., Cookenboo, H., 1999. Petrology of peridotite and pyroxenite xenoliths from the Jericho kimberlite: Implications for the thermal state of the mantle beneath the Slave craton, Northern Canada. J Petrol 40, 79-104.

Kopylova, M.G., Caro, G., 2004. Mantle Xenoliths from the Southeastern Slave Craton: Evidence for Chemical Zonation in a Thick, Cold Lithosphere. Journal of Petrology 45, 1045-1067.

Lassiter, J.C., 2003. Rhenium volatility in subaerial lavas: constraints from subaerial and submarine portions of the HSDP-2 Mauna Kea drillcore. Earth and Planetary Science Letters 214, 311-325.

LeCheminant, A.N., Heaman, L.M., 1989. Mackenzie igneous events, Canada: Middle Proterozoic hotspot magmatism associated with ocean opening. Earth and Planetary Science Letters 96, 38-48.

LeCheminant, A.N., Rainbird, R.H. and Villeneuve, M.E., 1996. Precambrian geology of northern Wellington Inlier, Victoria Island, Northwest Territories: in Current Research 1996-C; Geological Survey of Canada, p. 1-10.

Liu, C.Z., Snow, J.E., Hellebrand, E., Brugmann, G., von der Handt, A., Buchl, A., Hofmann, A.W., 2008. Ancient, highly heterogeneous mantle beneath Gakkel ridge, Arctic Ocean. Nature 452, 311-316.

Liu, J., Pearson, D.G., 2014. Rapid, precise and accurate Os isotope ratio measurements of nanogram to sub-nanogram amounts using multiple Faraday collectors and amplifiers equipped with 10^{12} Ω resistors by N-TIMS. Chemical Geology 363, 301-311.

Liu, J., Riches, A.J.V., Pearson, D.G., Luo, Y., Kienlen, B., Kjarsgaard, B.A., Stachel, T., Armstrong, J.P., 2016. Age and evolution of the deep continental root beneath the central Rae craton, northern Canada. Precambrian Research 272, 168-184.

Liu, J., Rudnick, R.L., Walker, R.J., Xu, W.-l., Gao, S., Wu, F.-y., 2015a. Big insights from tiny peridotites: Evidence for persistence of Precambrian lithosphere beneath the eastern North China Craton. Tectonophysics 650, 104-112.

Liu, J., Scott, J.M., Martin, C.E., Pearson, D.G., 2015b. The longevity of Archean mantle residues in the convecting upper mantle and their role in young continent formation. Earth and Planetary Science Letters 424, 109-118.

Liu, J.G., Rudnick, R.L., Walker, R.J., Gao, S., Wu, F.Y., Piccoli, P.M., 2010. Processes controlling highly siderophile element fractionations in xenolithic peridotites and their influence on Os isotopes. Earth and Planetary Science Letters 297, 287-297.

Liu, J.G., Rudnick, R.L., Walker, R.J., Gao, S., Wu, F.Y., Piccoli, P.M., Yuan, H.L., Xu, W.L., Xu, Y.G., 2011. Mapping lithospheric boundaries using Os isotopes of mantle xenoliths: an example from the North China Craton. Geochimica et Cosmochimica Acta 75, 3881-3902.

Lorand J. P., Alard O. and Luguet A., 2010. Platinum-group element micronuggets and refertilization process in Lherz orogenic peridotite (northeastern Pyrenees, France). Earth and Planetary Science Letters 289, 298-310.

Lorand J. P., Alard O., Luguet A. and Keays R. R., 2003a. Sulfur and selenium systematics of the subcontinental lithospheric mantle: Inferences from the Massif Central xenolith suite (France). Geochimica et Cosmochimica Acta 67, 4137-4151.

Lorand J. P., Delpech G., Gregoire M., Moine B., O'Reilly S. Y. and Cottin J. Y., 2004. Platinum-group elements and the multistage metasomatic history of Kerguelen lithospheric mantle (South Indian Ocean). Chemical Geology 208, 195-215.

Lorand J. P. and Luguet A., 2016. Chalcophile and Siderophile Elements in Mantle Rocks: Trace Elements Controlled By Trace Minerals. Rev Mineral Geochem 81, 441-488.

Lorand J. P., Luguet A. and Alard O., 2008. Platinum-group elements: A new set of key tracers for the earth's interior. Elements 4, 247-252.

Lorand J. P., Reisberg L. and Bedini R. M., 2003b. Platinum-group elements and melt percolation processes in Sidamo spinel peridotite xenoliths, Ethiopia, East African Rift. Chemical Geology 196, 57-75.

Luguet, A., Behrens, M., Pearson, D.G., Konig, S., Herwartz, D., 2015. Significance of the whole rock Re-Os ages in cryptically and modally metasomatised cratonic peridotites: Constraints from HSE-Se-Te systematics. Geochimica et Cosmochimica Acta 164, 441-463.

Luguet A., Alard O., Lorand J. P., Pearson N. J., Ryan C. and O'Reilly S. Y., 2001. Laser-ablation microprobe (LAM.-ICPMS unravels the highly siderophile element geochemistry of the oceanic mantle. Earth and Planetary Science Letters 189, 285-294.

Luguet A., Horan M. F., Shirey S. B., Lorand J. P. and Carlson R. W., 2004. Partitioning of highly siderophile elements (HSE. in very refractory peridotites. Geochimica et Cosmochimica Acta 68, A549-A549.

Luguet A., Lorand J. P. and Seyler M., 2003. Sulfide petrology and highly siderophile element geochemistry of abyssal peridotites: A coupled study of samples from the Kane Fracture

Zone (45 degrees W 23 degrees 20N, MARK Area, Atlantic Ocean). Geochimica et Cosmochimica Acta 67, 1553-1570.

Luguet, A., Jaques, A.L., Pearson, D.G., Smith, C.B., Bulanova, G.P., Roffey, S.L., Rayner, M.J., Lorand, J.P., 2009. An integrated petrological, geochemical and Re-Os isotope study of peridotite xenoliths from the Argyle lamproite, Western Australia and implications for cratonic diamond occurrences. Lithos 112, 1096-1108.

Luguet, A., Shirey, S.B., Lorand, J.P., Horan, M.F., Carlson, R.W., 2007. Residual platinum-group minerals from highly depleted harzburgites of the Lherz massif (France) and their role in HSE fractionation of the mantle. Geochimica et Cosmochimica Acta 71, 3082-3097.

Luguet, A. and Reisberg, L., 2016. Highly siderophile element and ^{187}Os signatures in non–cratonic basalt–hosted peridotite xenoliths: Unravelling the origin and evolution of the post-Archean lithospheric mantle. Rev Mineral Geochem 81, 305–367.

MacGregor, I.D., 1975, Petrologic and thermal structure ofthe upper mantle beneath South Africa in the Cretaceous: Physics and Chemistry of the Earth 9.

Mallmann, G., O'Neill, H.S.C., 2007. The effect of oxygen fugacity on the partitioning of Re between crystals and silicate melt during mantle melting. Geochimica et Cosmochimica Acta 71, 2837-2857.

Marchesi C., Dale C. W., Garrido C. J., Pearson D. G., Bosch D., Bodinier J.-L., Gervilla F. and Hidas K., 2014. Fractionation of highly siderophile elements in refertilized mantle: Implications for the Os isotope composition of basalts. Earth and Planetary Science Letters 400, 33-44.

Mather, K.A., Pearson, D.G., McKenzie, D., Kjarsgaard, B.A., Priestley, K., 2011. Constraints on the depth and thermal history of cratonic lithosphere from peridotite xenoliths, xenocrysts and seismology. Lithos 125, 729-742.

McCoy-West, A.J., Bennett, V.C., Puchtel, I.S., Walker, R.J., 2013. Extreme persistence of cratonic lithosphere in the southwest Pacific: Paleoproterozoic Os isotopic signatures in Zealandia. Geology 41 (2), 231–234.

McLean, H., Banas, A., Creighton, S., Whiteford, S., Luth, R.W., Stachel, T., 2007. Garnet xenocrysts from the Diavik mine, NWT, Canada: Composition, color, and paragenesis. The Canadian Mineralogist 45(5), 1131-1145.

McDonough, W.F., Sun, S.S., 1995. The composition of the Earth. Chemical Geology 120, 223-253.

Medaris, G., Wang, H., Jelínek, E., Mihaljevič, M., Jakeš, P., 2005. Characteristics and origins of diverse Variscan peridotites in the Gföhl Nappe, Bohemian Massif, Czech Republic. Lithos 82, 1-23.

Meibom, A., Sleep, N.H., Chamberlain, C.P., Coleman, R.G., Frei, R., Hren, M.T., Wooden, J.L., 2002. Re-Os isotopic evidence for long-lived heterogeneity and equilibration processes in the Earth's upper mantle. Nature 419, 705-708.

Nimis, P., Taylor, W.R., 2000. Single clinopyroxene thermobarometry for garnet peridotites. Part I. Calibration and testing of a Cr-in-Cpx barometer and an enstatite-in-Cpx thermometer. Contributions to Mineralogy and Petrology 139, 541-554.Okulitch, A.V., Packard, J.J., Zolnai, A.I., 1986. Evolution of the Boothia Uplift, arctic Canada. Canadian Journal of Earth Sciences 23, 350-358.

Ootes, L., Davis, W. J., Jackson, V. A. and van Breemen, O., 2015. Chronostratigraphy of the Hottah terrane and Great Bear magmatic zone of Wopmay Orogen, Canada, and exploration of a terrane translation model. Canadian Journal of Earth Sciences 52, 1062-1092.

Paton, C., Hellstrom, J., Paul, B., Woodhead, J., Hergt, J., 2011. Iolite: Freeware for the visualisation and processing of mass spectrometric data. Journal of Analytical Atomic Spectrometry 26, 2508–2518.

Pearson, D.G., Carlson, R.W., Shirey, S.B., Boyd, F.R., Nixon, P.H., 1995. Stabilization of Archean Lithospheric Mantle - a Re-Os Isotope Study of Peridotite Xenoliths from the Kaapvaal Craton. Earth and Planetary Science Letters 134, 341-357.

Pearson, D.G., 1999. The age of continental roots. Lithos 48 (1), 171-194.

Pearson, D.G., Irvine, G.J., Carlson, R.W., Kopylova, M.G., Ionov, D.A., 2002. The development of lithospheric keels beneath the earliest continents: time constraints using PGE and Re-Os isotope systematics. Geological Society, London, Special Publications 199, 65-90.

Pearson, D.G., Parman, S.W., Nowell, G.M., 2007. A link between large mantle melting events and continent growth seen in Osmium isotopes. Nature 449, 202-205.

Pearson, D.G., Canil, D., Shirey, S.B., 2014. 3.5 - Mantle Samples Included in Volcanic Rocks: Xenoliths and Diamonds, in: Holland, H.D., Turekian, K.K. (Eds.), Treatise on Geochemistry (Second Edition). Elsevier, Oxford, pp. 169-253.

Pearson, D.G., Irvine, G.J., Ionov, D.A., Boyd, F.R., Dreibus, G.E., 2004. Re-Os isotope systematics and platinum group element fractionation during mantle melt extraction: a study of massif and xenolith peridotite suites. Chemical Geology 208, 29-59.

Pearson, D.G., Wittig, N., 2008. Formation of Archaean continental lithosphere and its diamonds: the root of the problem. Journal of the Geological Society 165, 895-914.

Pearson, D.G., Wittig, N., 2014. The formation and evolution of the subcontinental mantle lithosphere - evidence from mantle xenoliths. Treatise of Geochemistry, Volume 3: The Mantle and Core, Chapter 3.6, 255–292.

Pearson, D.G., Woodland, S.J., 2000. Solvent extraction/anion exchange separation and determination of PGEs (Os, Ir, Pt, Pd, Ru) and Re-Os isotopes in geological samples by isotope dilution ICP-MS. Chemical Geology 165, 87-107.

Pearson, N.J., Griffin, W.L., Doyle, B.J., O'Reilly, S.,van Achterburgh, E. and Kivi, K., 1999. Xenoliths from kimberlite pipes of the Lac de Gras area, Slave craton, Canada. Proceedings of the 7th Kimberlite Conference, J.J. Gurney et al., (eds), Red Roof, Cape Town, p. 644-658.

Pilkington, M., and Saltus, R.W., 2009. The Mackenzie River magnetic anomaly, Yukon and Northwest Territories, Canada - evidence for Early Proterozoic magmatic arc crust at the edge of the North American craton. Tectonophysics 478.

Potts, P.J., 1992. A Handbook of Silicate Rock Analysis: New York City, New York, Spinger.

Rao, N.V.C., Creaser, R.A., Lehmann, B., Panwar, B.K., 2013. Re–Os isotope study of Indian kimberlites and lamproites: Implications for mantle source regions and cratonic evolution. Chemical Geology 353, 36-47.

Rehkämper, M., Halliday, A.N., Barfod, D. and Fitton, J.G., 1997 Platinum-group element abundance patterns in different mantle environments. Science 278, 1595-1598.

Reisberg L., Lorand J. P. and Bedini R. M., 2004. Reliability of Os model ages in pervasively metasomatized continental mantle lithosphere: a case study of Sidamo spinel peridotite xenoliths (East African Rift, Ethiopia). Chemical Geology 208, 119-140.

Rudnick R. L., McDonough W. F. and Chappell B. W., 1993. Carbonatite metasomatism in the northern Tanzanian mantle: Petrographic and geochemical characteristics. Earth and Planetary Science Letters 114, 463-475.

Rudnick, R.L., Walker, R.J., 2009. Interpreting ages from Re–Os isotopes in peridotites Lithos 112S, 1083-1095.

Sand, K.K., Waight, T., Pearson, D.G., Nielsen, T.F.D., Makovicky, D. E. and Hutchison, M. T., 2009. The lithospheric mantle below southern West Greenland: a geothermobarometric approach to diamond potential and mantle stratigraphy. Lithos 112S, 1155–1166.

Schaeffer, A.J., Lebedev, S., 2014. Imaging the North American continent using waveform inversion of global and USArray data. Earth and Planetary Science Letters 402, 26-41.

Schulze, D.J., 1989. Constraints on the abundance of eclogite in the upper mantle. Journal of Geophysical Research: Solid Earth 94, 4205-4212.

Shimizu, N., Richardson, S.H., 1987. Trace-Element Abundance Patterns of Garnet Inclusions in Peridotite-Suite Diamonds. Geochimica et Cosmochimica Acta 51, 755-758.

Shirey, S.B., Walker, R.J., 1998. The Re-Os isotope system in cosmochemistry and high-temperature geochemistry. Annual Review of Earth and Planetary Sciences 26, 423-500.

Shu, Q., Brey, G.P., 2015. Ancient mantle metasomatism recorded in subcalcic garnet xenocrysts: Temporal links between mantle metasomatism, diamond growth and crustal tectonomagmatism. Earth and Planetary Science Letters 418, 27-39.

Simon, N.S.C., Carlson, R.W., Pearson, D.G., Davies, G.R., 2007. The origin and evolution of the Kaapvaal cratonic lithospheric mantle. Journal of Petrology 48, 589-625.

Simon, N.S.C., Irvine, G.J., Davies, G.R., Pearson, D.G., Carlson, R.W., 2003. The origin of garnet and clinopyroxene in "depleted" Kaapvaal peridotites. Lithos 71, 289-322.

Stacey, R.A., 1971. Interpretation of the gravity anomaly at Darnley Bay, Northwest Territories (N.W.T.). Canadian Journal of Earth Science 8, 1037-1042.

Stachel, T., Viljoen, K.S., Brey, G., Harris, J.W., 1998. Metasomatic processes in lherzolitic and harzburgitic domains of diamondiferous lithospheric mantle: REE in garnets from xenoliths and inclusions in diamonds. Earth and Planetary Science Letters 159, 1-12.

Stagno, V., Ojwang, D.O., McCammon, C.A., Frost, D.J., 2013. The oxidation state of the mantle and the extraction of carbon from Earth's interior. Nature 493, 84-+.

Sun, S.-S., McDonough, W.F., 1989. Chemical and isotopic systematics of oceanic basalts: implications formantle composition andprocesses. Geological Society, London, Special Publications 42, 313–345.

Sweeney R. J., Green D. H. and Sie S. H., 1992. Trace and minor element partitioning between garnet and amphibole and carbonatitic melt. Earth and Planetary Science Letters 113, 1-14.

Tappe, S., Brand, N.B., Stracke, A., van Acken, D., Liu, C.-Z., Strauss, H., Wu, F.-Y., Luguet, A. and Mitchell, R.H., 2017. Plates or plumes in the origin of kimberlites: U/Pb perovskite and Sr-Nd-Hf-Os-C-O isotope constraints from the Superior craton (Canada). Chemical Geology 455, 57-83.

Thorsteinsson, R., and Tozer, E.T., 1962. Banks, Victoria and Stefansson Islands, Arctic Archipelago, Memoirs 330, Geological Survey of Canada, p. 85.

van der Hilst, R.D., Kennett, B.L.N., Shibutani, T.,1998.Upper mantle structure beneath Australia from portable array deployments. Geodynamics Series, volume 26, pp. 39 - 57

van Acken D., Becker H., Walker R. J., McDonough W. F., Wombacher F., Ash R. D. and Piccoli P. M., 2010a. Formation of pyroxenite layers in the Totalp ultramafic, massif (Swiss Alps. - Insights from highly siderophile elements and Os isotopes. Geochimica et Cosmochimica Acta 74, 661-683.

van Acken, D., Becker, H., Hammerschmidt, K., Walker, R.J. and Wombacher, F., 2010b. Highly siderophile elements and Sr-Nd isotopes in refertilized mantle peridotites - A case study from the Totalp ultramafic body, Swiss Alps. Chemical Geology 276, 257-268.

van Acken, D., Luguet, A., Pearson, D.G., Nowell, G.M., Fonseca, R.O.C., Nagel, T.J. and Schulz, T., 2017 Mesoarchean melting and Neoarchean to Paleoproterozoic metasomatism during the formation of the cratonic mantle keel beneath West Greenland. Geochimica et Cosmochimica Acta 203, 37-53.

van der Meer, Q.H.A., Klaver, M., Reisberg, L., Riches, A.J.V. and Davies, G.R., 2017 Preservation of an Archaean whole rock Re-Os isochron for the Venetia lithospheric mantle: Evidence for rapid crustal recycling and lithosphere stabilisation at 3.3 Ga. Geochimica et Cosmochimica Acta 216, 242-263.

Wainwright A. N., Luguet A., Fonseca R. O. C. and Pearson D. G., 2015. Investigating metasomatic effects on the 187Os isotopic signature: A case study on micrometric base metal sulphides in metasomatised peridotite from the Letlhakane kimberlite (Botswana). Lithos 232, 35-48.

Walker, R.J., Shirey, S.B., Hanson, G.N., Rajamani, V., Horan, M.F., 1989. Re-Os, Rb-Sr, and O Isotopic Systematics of the Archean Kolar Schist Belt, Karnataka, India. Geochimica et Cosmochimica Acta 53, 3005-3013.

Wang, Z., Becker, H. (2014). Abundances of sulfur, selenium, tellurium, rhenium and platinum‐group elements in eighteen reference materials by isotope dilution sector‐field ICP‐MS and negative TIMS. Geostandards and Geoanalytical Research, 38(2), 189-209.

Wittig, N., Pearson, D.G., Webb, M., Ottley, C.J., Irvine, G.J., Kopylova, M., Jensen, S.M., Nowell, G.M., 2008. Origin of cratonic lithospheric mantle roots: A geochemical study of peridotites from the North Atlantic Craton, West Greenland. Earth and Planetary Science Letters 274, 24-33.

Xiong, Y., Wood, S.A., 1999. Experimental determination of the solubility of ReO2 and the dominant oxidation state of rhenium in hydrothermal solutions. Chemical Geology 158, 245-256.

Yaxley G. M., Crawford A. J. and Green D. H., 1991. Evidence for carbonatite metasomatism in spinel peridotite xenoliths from western Victoria, Australia. Earth and Planetary Science Letters 107, 305-317.

Yudovskaya, M.A., Tessalina, S., Distler, V.V., Chaplygin, I.V., Chugaev, A.V., Dikov, Y.P., 2008. Behavior of highly-siderophile elements during magma degassing: A case study at the Kudryavy volcano. Chemical Geology 248, 318-341.

Figure captions

Figure 1. Simplified geological map of Canada (modified after Kjarsgaard, 1996 and Berman et al., 2005), showing the peridotite xenolith localities (Parry Peninsula and Central Victoria Island). Major Neoarchean to Paleoproterozoic orogenic belts (Wp - Wopmay orogeny including the collisional arc Hottah terrane and the Great Bear magmatic zone, Tmz-Ttz - Taltson-Thelon orogeny, Trans-Hudson orogeny) are highlighted.

Figure 2. Comparison of the peridotites from Parry Peninsula and Central Victoria Island with other global peridotites: Olivine Mg# (100 x Mg/(Mg + Fe)) versus olivine modal abundance and olivine Mg# versus spinel Cr# (100 x Cr/(Cr + Al)). The field labelled "Greenland cratonic peridotites" contains data from Ubekendt, Wiedemann, and Sarfartoq (Bernstein et al., 1998, 2006; Sand et al., 2009) suites. 'OSMA': olivine-spinel mantle array from Arai (1994). Given the large variations in spinel Cr# of the cratonic peridotites, the error bar marks the total range, whereas 1σ is plotted for the peridotite suites studied. The large symbols with initial letters indicate the average for each suite with 1σ error.

Figure 3. Cr_2O_3-CaO compositions of garnets from Central Victoria Island (A) and Parry Peninsula (B) peridotites and till concentrate following the classification of Grütter et al. (2004). Isobars are from Cr-in-garnet barometer P38 from Grütter et al. (2006). GDC: graphite-diamond constraint line. C. Mg#-Al_2O_3 contents of clinopyroxene. D. Mg#-Cr# of spinel. Open field is for minerals from global non-cratonic peridotites and gray field for minerals from global cratonic peridotites in the literature.

Figure 4. Chondrite-normalized rare earth element (REE) patterns for garnet from Central Victoria Island xenolithic peridotites (A), till concentrate (B and C). Based on the REE patterns,

they are divided into four Types (1-4). See text for details. Chondrite values are after Sun and McDonough (1989).

Figure 5. Diagrams of Zr versus Y (A; after Griffin et al., 1999) and Zr/Hf versus Ti/Eu (B; Yaxley et al., 1991; Rudnick et al., 1993; Sweeney et al., 1992) of the peridotitic garnets from this study. The fields of carbonatitic metasomatism and kimberlitic melt metasomatism are referred to Shu and Brey (2015) and reference therein. Symbols are kept the same in the remaining figures.

Figure 6. Whole-rock major Al_2O_3 versus CaO element compositions of peridotite xenoliths from Parry Peninsula and Central Victoria Island. CVI peridotites are divided into five groups based on HSE patterns (see detail in text; **Fig. 7**), and some are noted for carbonation (CaO>3 wt. %, Ca/Al >1.6) or Al enrichment (Al_2O_3 around 4 wt. %). Also shown are the typical refractory cratonic peridotites (olivine Fo > 91; Pearson and Wittig, 2008 and references therein) and the composition of the primitive upper mantle (PUM; McDonough and Sun, 1995). The straight line delineates the approximation trend of melt depletion.

Figure 7. CI chondrite-normalized HSE patterns of peridotites from Central Victoria Island (A) (based on the absolute and relative HSE concentrations, these rocks can be divided into five groups with key features stated in the text) and Parry Peninsula (B. Whole rock; C. Olivine separate). CI chondrite values here and in the remaining figures are after Anders and Grevesse (1989) and Horan et al. (2003).

Figure 8. Pd_N/Ir_N versus Al_2O_3 (A) or CaO (B), concentration Ir versus Os (C; the regression line is conducted from all data) or Pt (D; the regression line is conducted from all data), Pd versus Pt (E), and Pd_N/Ir_N versus Pd_N/Ir_N (F). Also shown are the composition of PUM (McDonough and Sun, 1995; Becker et al., 2006).

Figure 9. Correlations between $^{187}Os/^{188}Os$ and HSE pattern groups (A), Al_2O_3 (B), CaO (C), Pd_N/Ir_N (D), 1/Os (E), and Os_N/Ir_N (F). Grey fields indicate the main range of $^{187}Os/^{188}Os$ ratios (i.e., 0.1132-0.1162).

Figure 10. A. Rhenium-Osmium isochron diagram. B. $^{187}Os/^{188}Os$ versus time in the mantle evolution framework. T=0 represents the measured data, and T=0.27 Ga represents the values corrected for the radiogenic ingrowth of ^{187}Os from ^{187}Re decay assuming all Re was added to the rock during the kimberlite eruption, and the T=0.27 Ga $^{187}Os/^{188}Os$ are used to calculate the rhenium-depletion model ages named as $T_{RDeruption}$ (Pearson et al., 1995). The mantle evolution is following a chondritic mantle using the ordinary chondrite numbers (modern $^{187}Re/^{188}Os = 0.422$ and $^{187}Os/^{188}Os = 0.1283$; Horan et al., 2003).

Figure 11. Osmium model ages: Histograms and probability density functions of rhenium depletion model ages ($T_{RDeruption}$) of Parry Peninsula (both whole rock and olivine separate; A) and Central Victoria Island (B) excluding the five Group D peridotites discussed in the text.

Figure 12. Single clinopyroxene thermobarometer: P-T data calculated using the method of Nimis and Taylor (2000) are fitted to define a mantle geotherm (solid line with shading representing the 2σ error envelope): A. Parry Peninsula with the combination of xenolith and till concentrate clinopyroxene; B. till concentrate clinopyroxene from Central Victoria Island; **Table S6**) using the FITPLOT (parameters are shown in **Table 3**) method of Mather et al. (2011). Only grains proven to be stoichiometric were used for calculations (**Fig. S8**). Grains deemed not from garnet peridotites or that failed to produce both pressure and temperature were omitted from further consideration. The reference geotherm for the Central Slave craton is from Grütter (2009). The diamond-graphite transitions of Kennedy and Kennedy (1976) and Day (2012) are plotted for reference.

Table Captions

Table 1. Highly siderophile element, Se and Te concentrations and Re-Os isotopic systematics for Central Victoria Island peridotites, and Parry Peninsula peridotites and their olivine separates.

Table 2. Summary of the CVI peridotite grouping based on the HSE characteristics

Table 3. FITPLOT parameters used for thermobarometry.

Liu et al. Figure 1

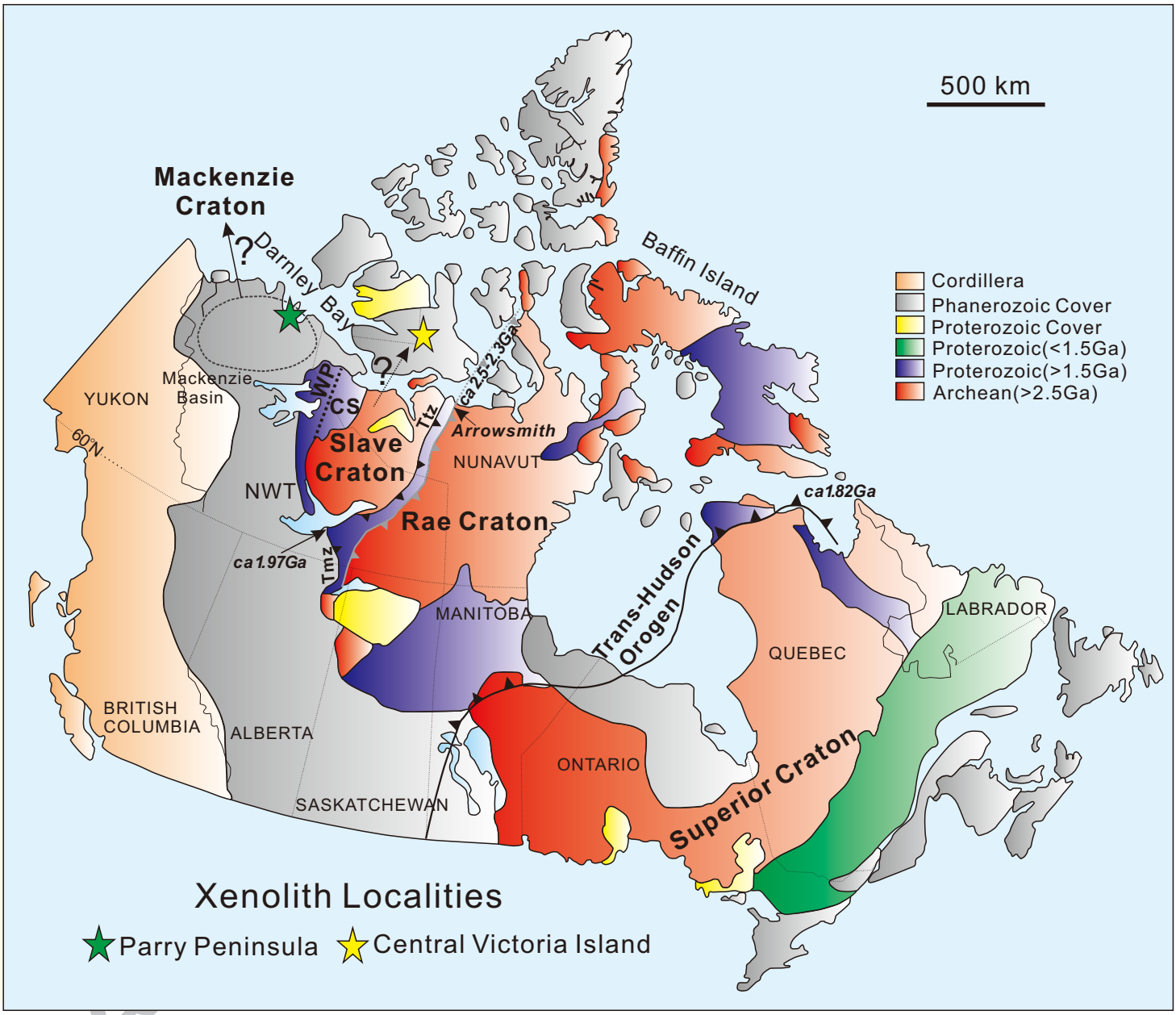

Liu et al. Figure 2

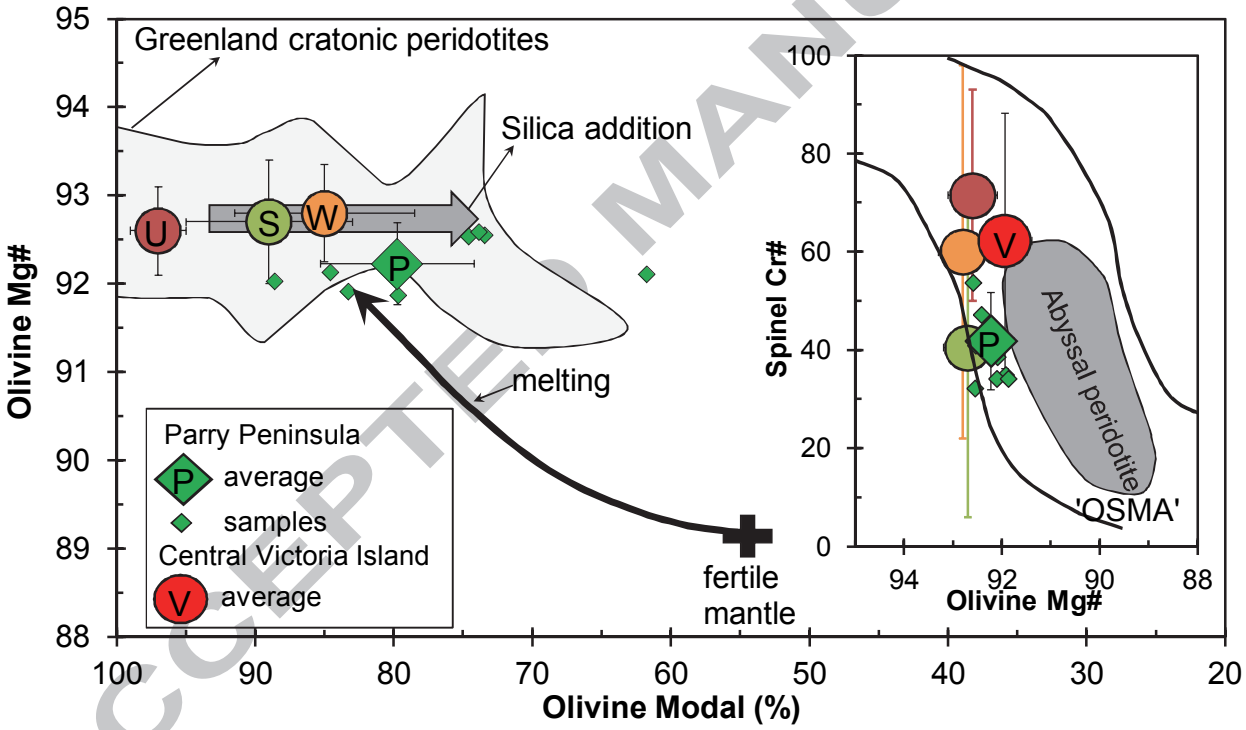

Liu et al. Figure 3

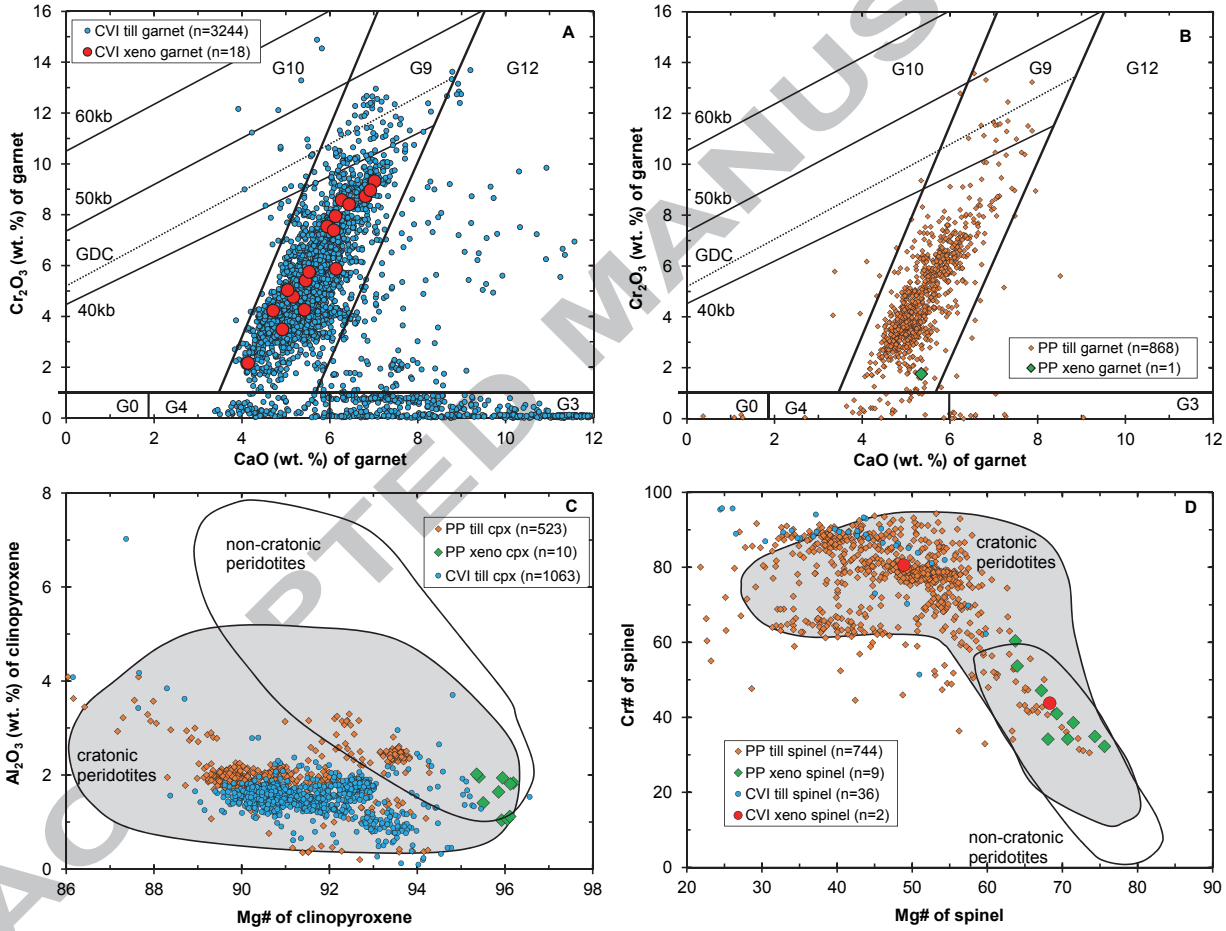

Liu et al. Figure 4

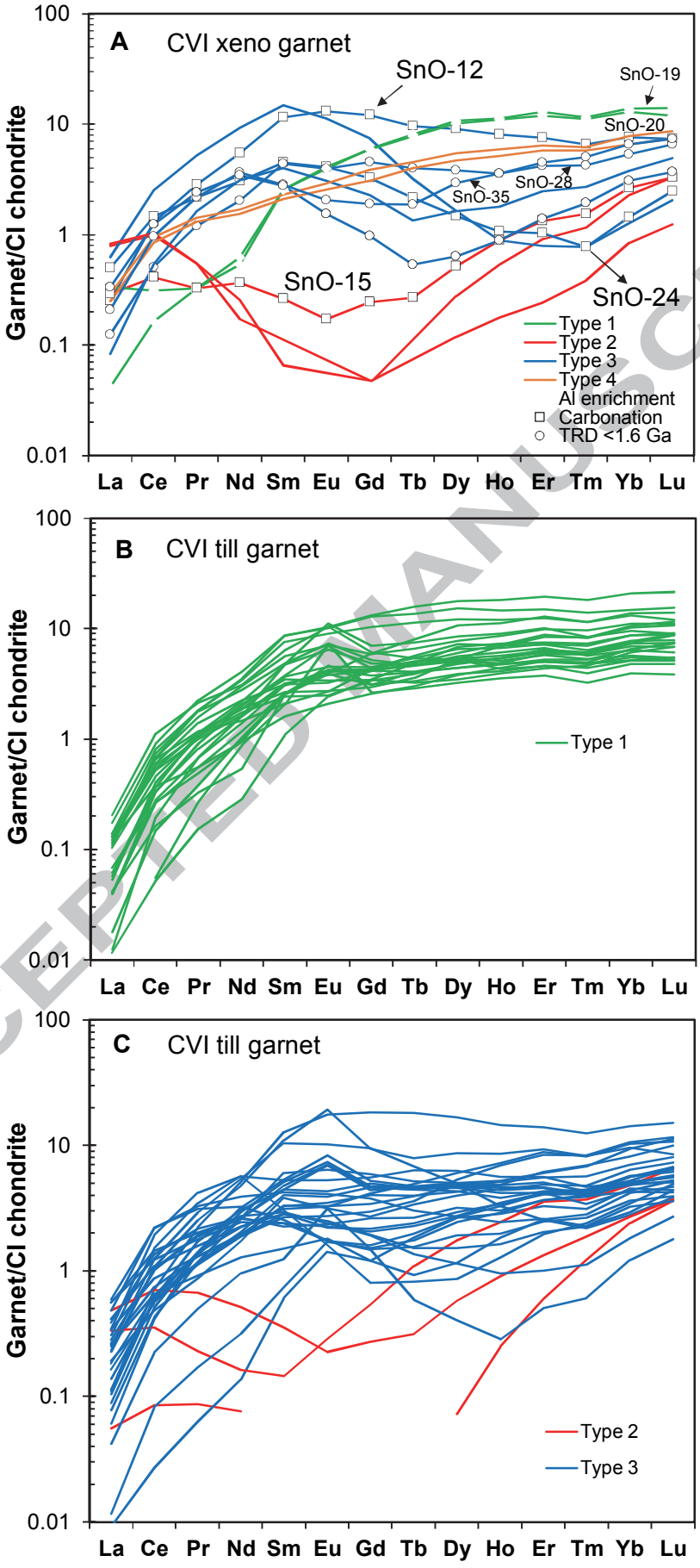

Liu et al. Figure 5

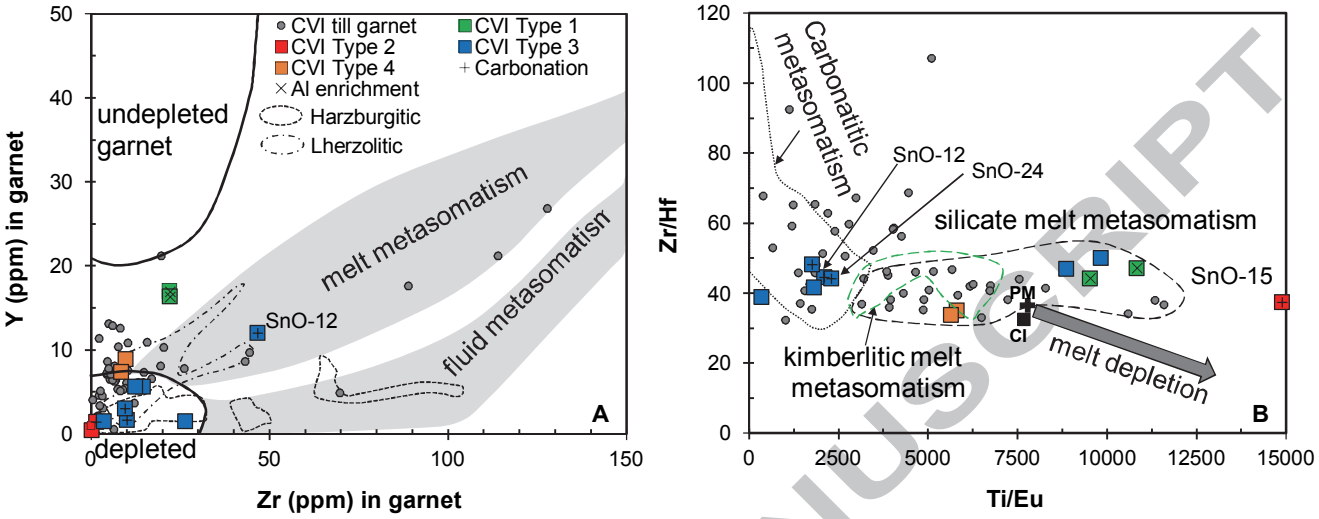

Liu et al. Figure 6

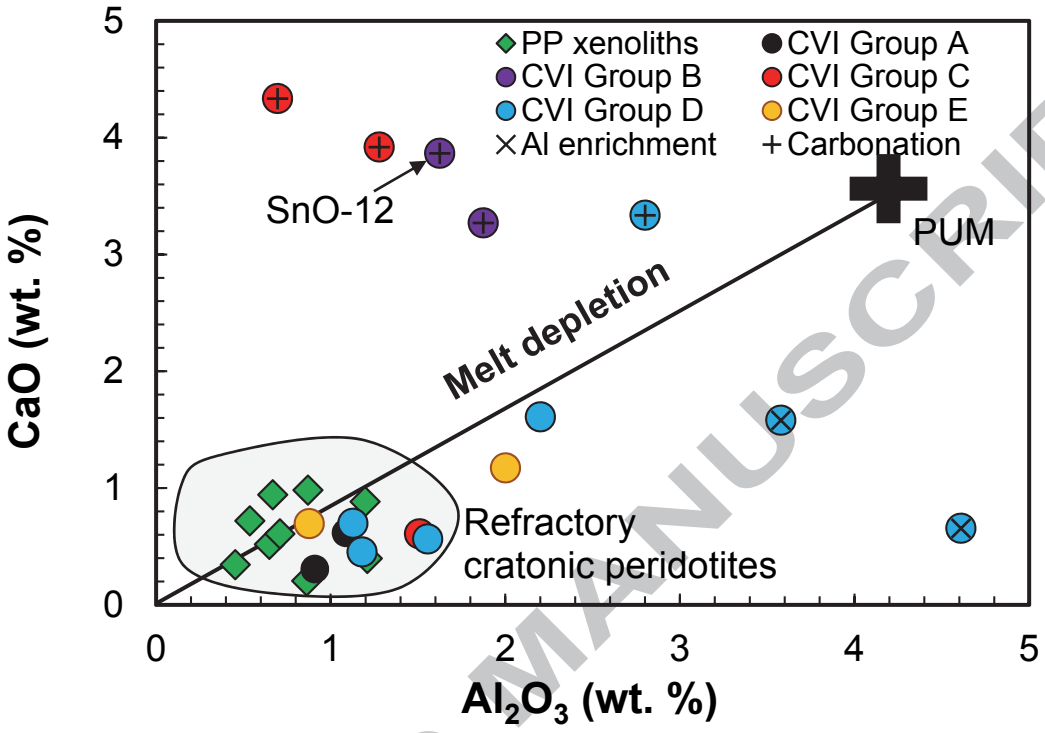

Liu et al. Figure 7

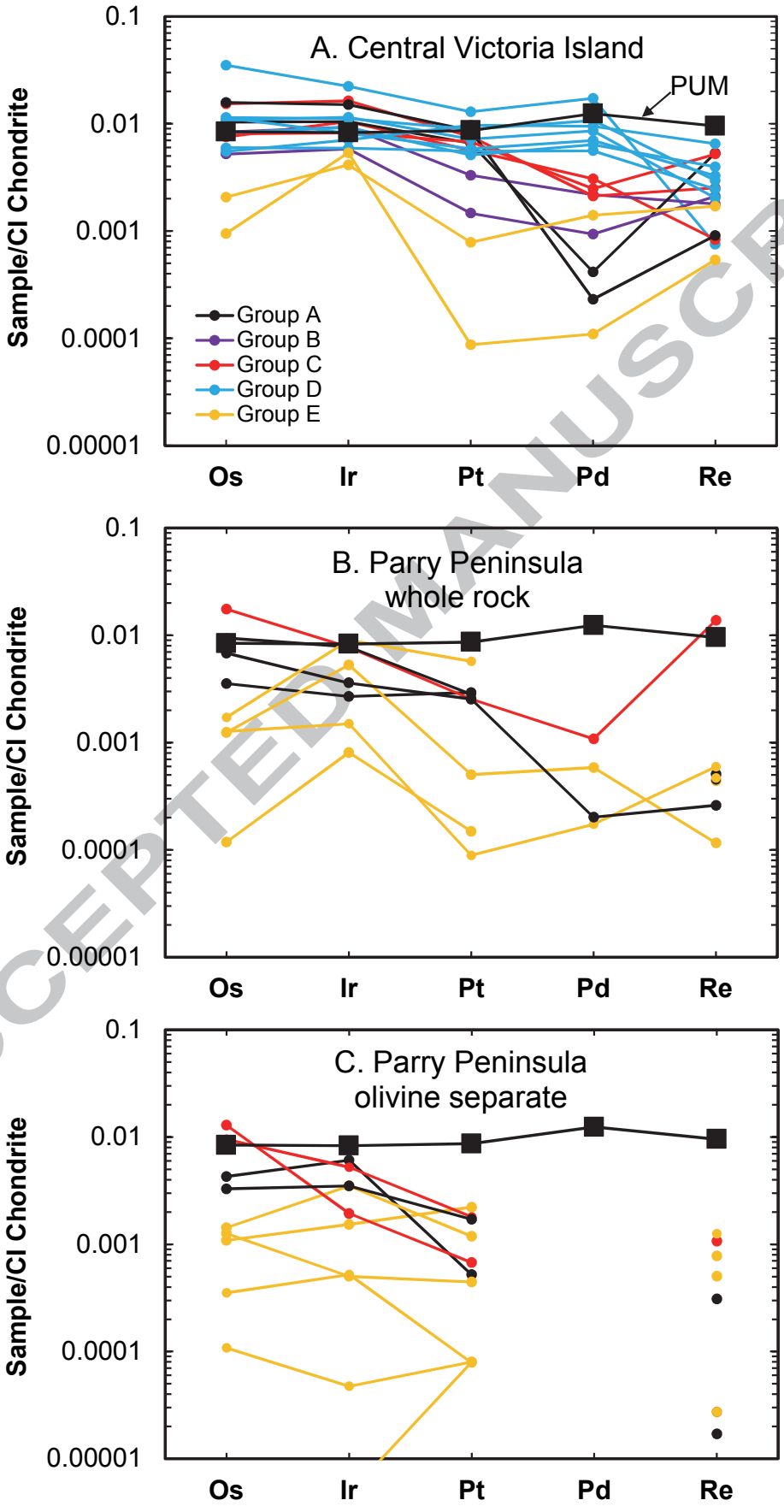

Liu et al. Figure 8

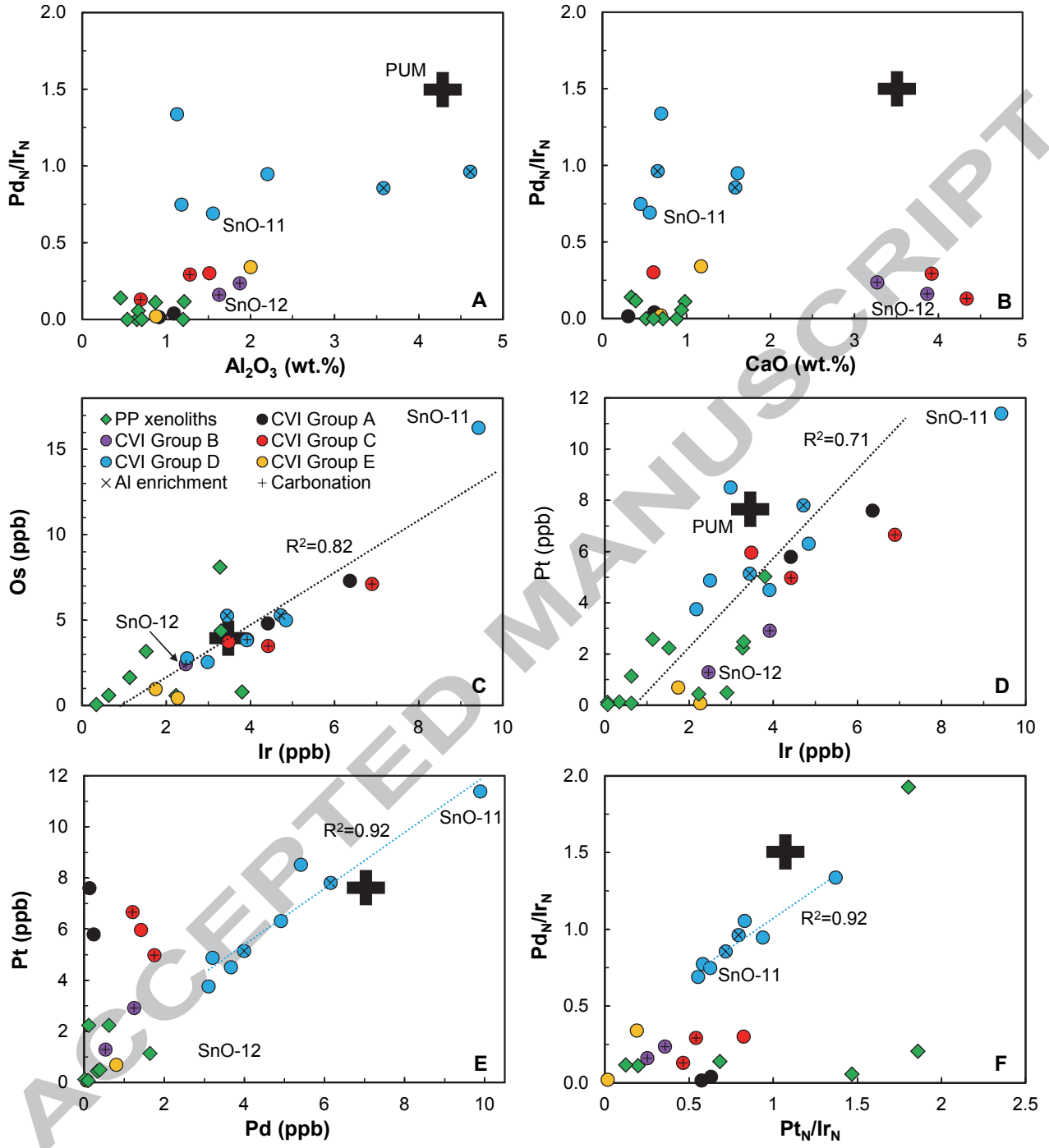

Liu et al. Figure 9

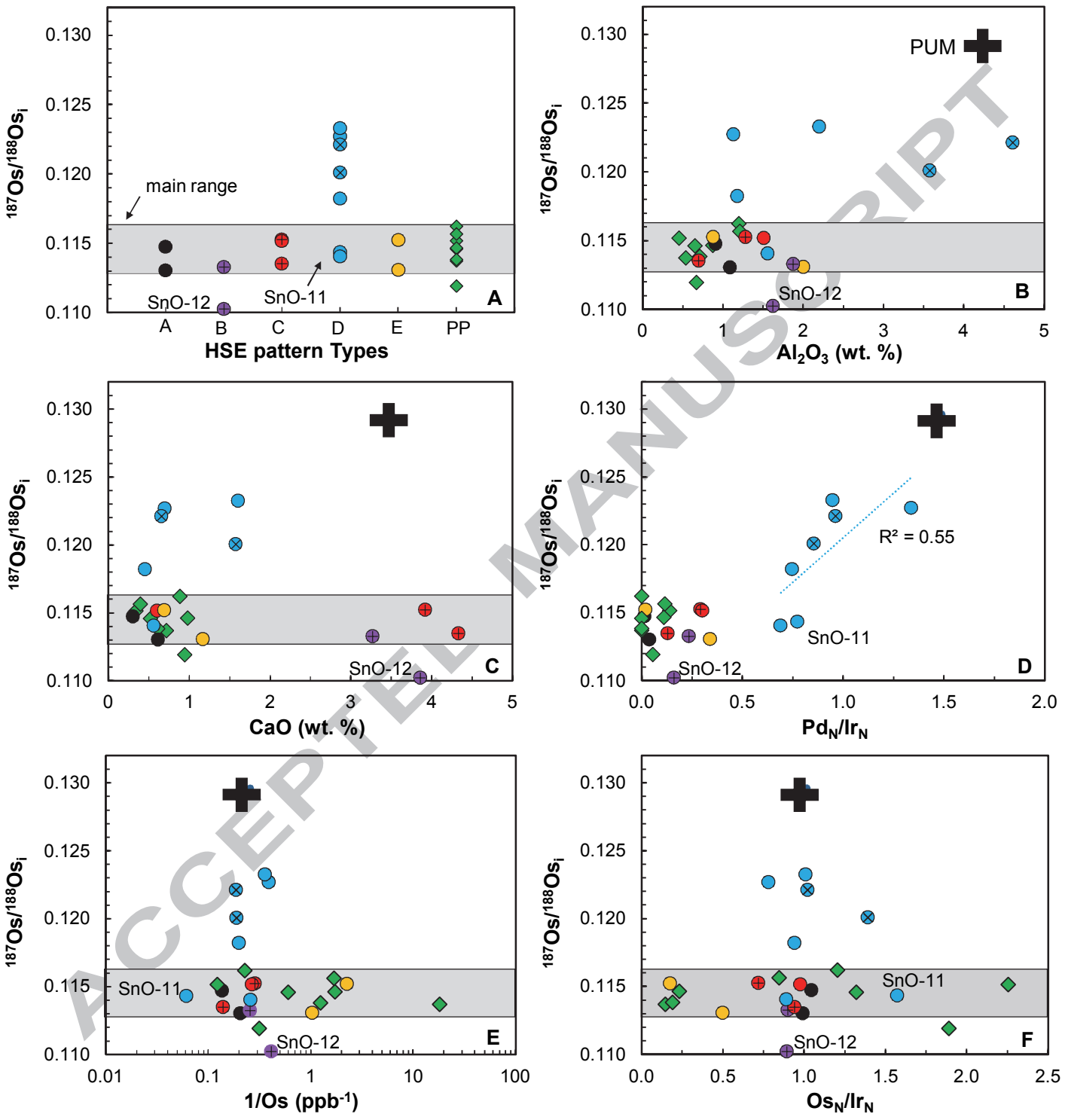

Liu et al. Figure 10

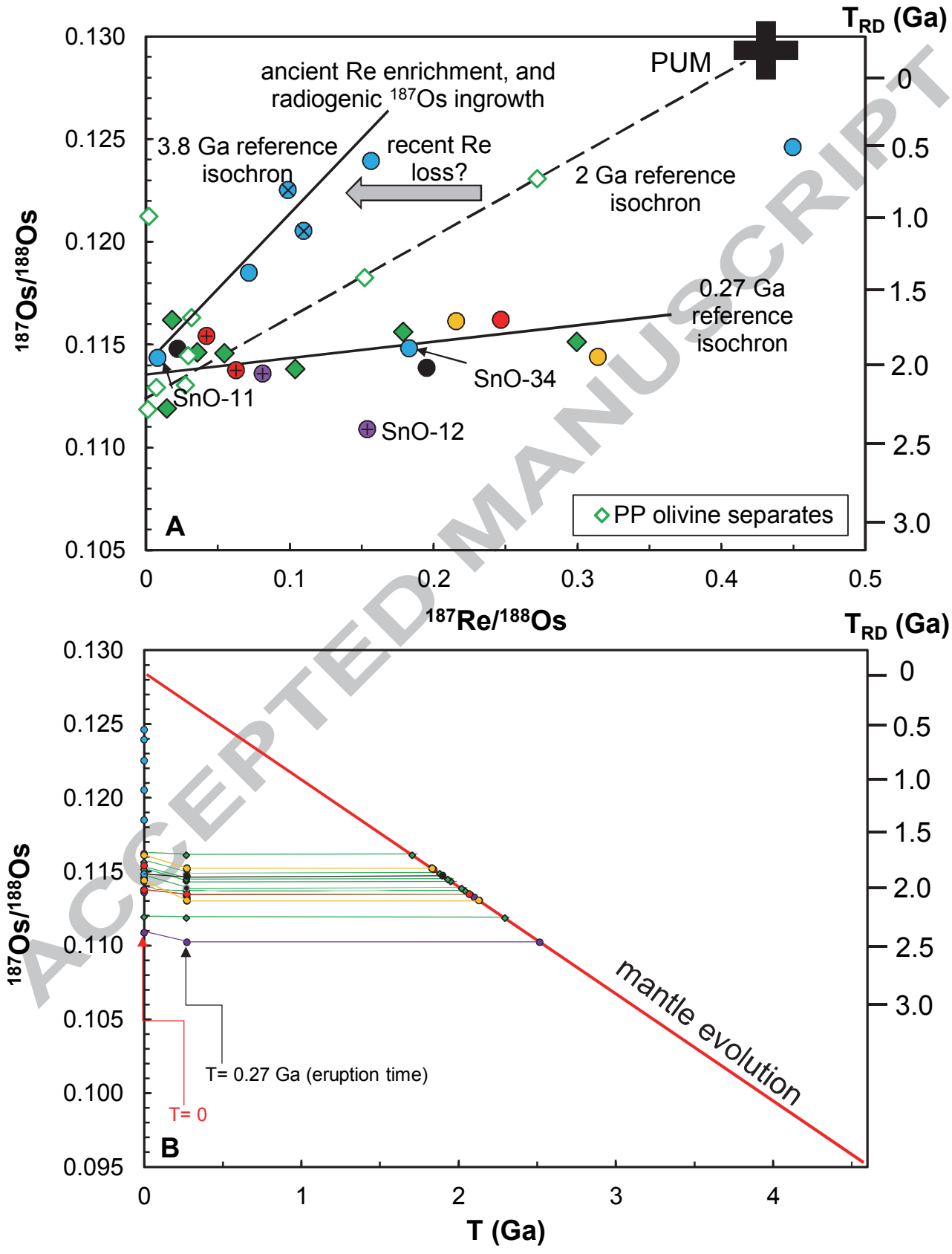

Liu et al. Figure 11

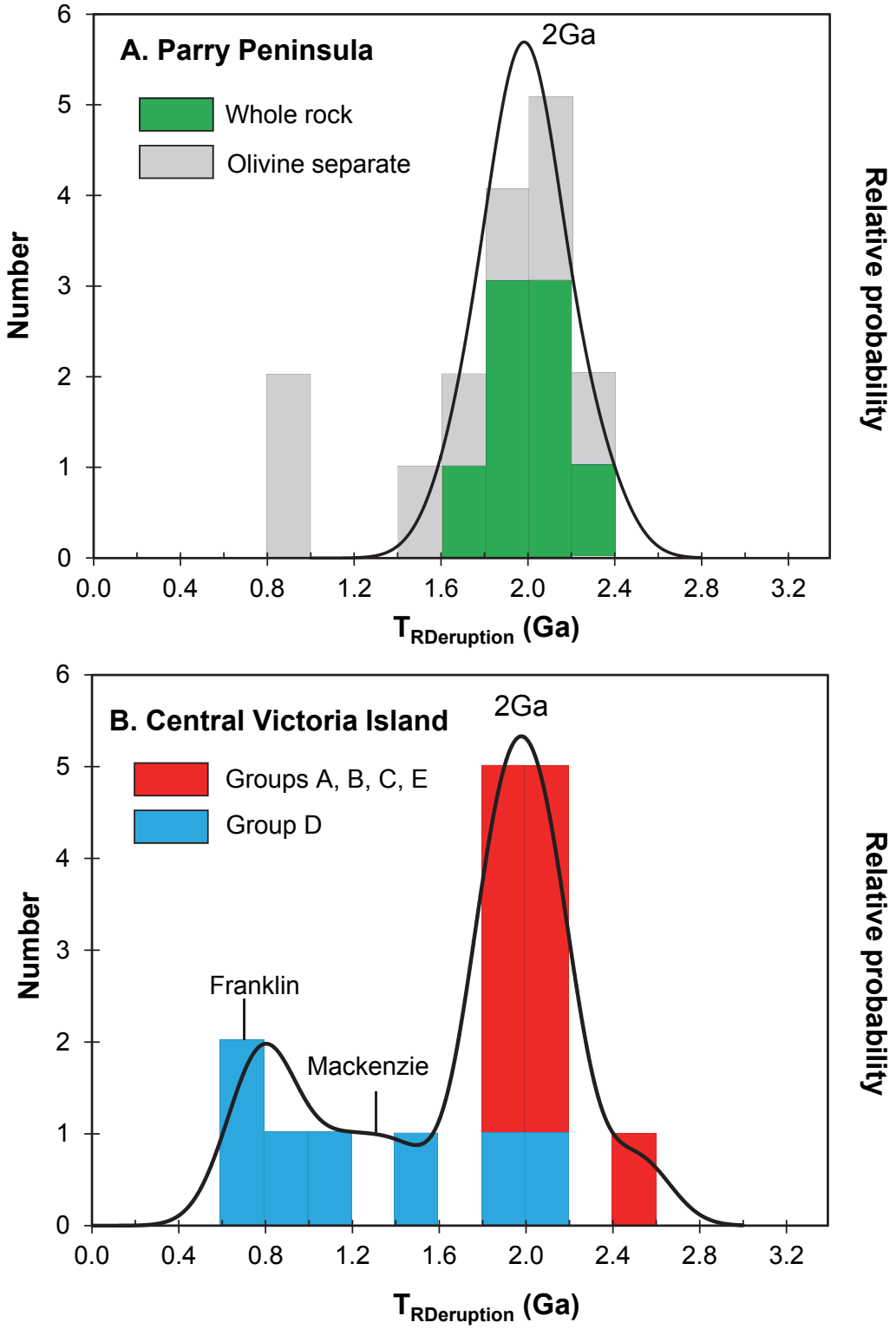

Liu et al., Figure 12

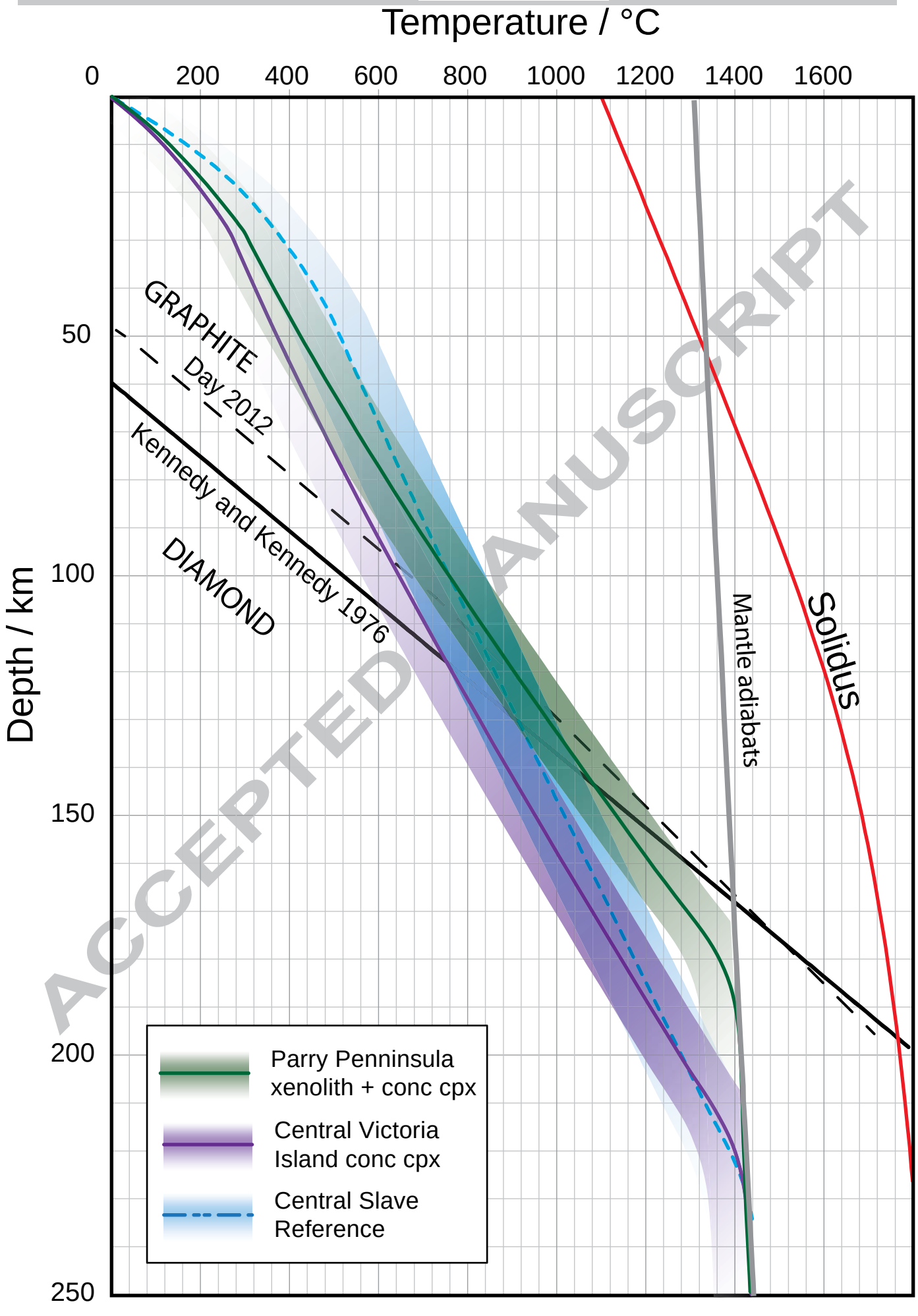

Table 1. Highly siderophile element, Se and Te concentrations and Re-Os isotopic systematics for Central Victoria Island peridotites, and Parry Peninsula peridotites and their olivine separates.

Sample	Al_2O_3 (wt. %)	CaO (wt. %)	Os (ppb)	Ir (ppb)	Ru (ppb)	Pt (ppb)	Pd (ppb)	Re (ppb)	Se (ppb)	Te (ppb)	$^{187}Re/^{188}Os$	$^{187}Os/^{188}Os$	2σ	$(^{187}Os/^{188}Os)i$	$T_{RDeruption}$ (Ga)	T_{MA} (Ga)
Central Victoria Island Whole Rock																
SnO-5			n.d.	n.d.	n.d.	n.d.	n.d.	n.d.	n.d.	0.83						
SnO-11			16.27	9.42		11.39	9.89	0.028			0.008	0.11437	0.00009	0.11433	1.95	1.99
SnO-12	1.63	3.86	2.42	2.46		1.29	0.54	0.077	16.4	15.66	0.15	0.11089	0.00005	0.11023	2.52	3.78
SnO-15	1.28	3.92	3.49	4.42		4.98	1.76	0.031	12.7	5.57	0.042	0.11542	0.00003	0.11524	1.83	2.00
SnO-15R				2.60	4.56	3.31	2.55	0.028								
SnO-17	1.13	0.70	2.56	2.99		8.51	5.41	0.239	n.d.	11.88	0.45	0.12463	0.00006	0.12269	0.79	-
SnO-19	4.61	0.65	5.30	4.72		7.81	6.16	0.109	23.4	10.24	0.099	0.12253	0.00003	0.12211	0.87	1.06
SnO-20	3.58	1.58	5.26	3.45		5.14	4.00	0.120	25.9	9.89	0.110	0.12054	0.00052	0.12007	1.16	1.47
SnO-20R				2.92	5.66	5.01	6.33	0.127								
SnO-21	1.87	3.27	3.88	3.92		2.91	1.25	0.065	b.d.l.	4.80	0.081	0.11361	0.00037	0.11326	2.10	2.53
SnO-21R				4.25	6.48	3.94	1.31	0.089								
SnO-24	0.70	4.33	7.12	6.89		6.66	1.21	0.093	n.d.	1.09	0.063	0.11376	0.00035	0.11350	2.07	2.38
SnO-24R				3.67	4.07	7.55	1.80	0.087								
SnO-26	2.00	1.17	0.96	1.75		0.69	0.81	0.063	n.d.	n.d.	0.31	0.11441	0.00010	0.11306	2.13	7.30
SnO-27	0.91	0.31	7.31	6.37		7.60	0.13	0.033	b.d.l.	0.93	0.022	0.11482	0.00074	0.11472	1.90	1.99
SnO-27R				4.70	1.01	8.10	0.21	0.016								
SnO-28	1.18	0.45	5.01	4.85		6.31	4.91	0.074	b.d.l.	2.06	0.072	0.11851	0.00050	0.11821	1.42	1.65
SnO-28R				6.48	14.99	7.24	4.21	0.05								
SnO-29				2.17	4.31	3.75	3.11	0.111	14.5	5.88						
SnO-32	1.09	0.62	4.81	4.42		5.79	0.24	0.196	7.4	9.45	0.195	0.11387	0.00081	0.11303	2.13	3.71
SnO-32R				3.25	3.37	4.76	2.97	0.196								
SnO-33	1.51	0.61	3.73	3.48		5.96	1.42	0.191	13.9	8.71	0.247	0.11622	0.00050	0.11516	1.84	4.01
SnO-33R				2.64	6.37	6.40	3.42	0.183								
SnO-34	1.56	0.56	3.83	3.91		4.50	3.66	0.146	b.d.l.	3.12	0.183	0.11483	0.00039	0.11404	1.99	3.30
SnO-34R				3.91	8.32	4.72	2.76	0.154								
SnO-35	2.20	1.61	2.77	2.50		4.87	3.21	0.090	n.d.	0.80	0.157	0.12394	0.00022	0.12326	0.71	0.98
SnO-35R				0.80	2.38	0.34	0.18	0.028								
SnO-36	0.88	0.69	0.44	2.27		0.08	0.06	0.020	b.d.l.	3.79	0.216	0.11614	0.00009	0.11521	1.83	3.44

Parry Peninsula Whole rock															
DB1A	0.65	0.52	1.64	1.13		2.57	b.d.l.	0.019	b.d.l.	0.35	0.055	0.11459	0.00046	0.11436	1.95	2.20
DB2D	0.54	0.72	0.05	0.34		0.13	b.d.l.	0.016			1.41	0.11371	0.00013	0.11371	2.04	-
DB2DR				0.06	0.49	0.12	0.02	0.005	b.d.l.	0.72						
DB3A	0.45	0.34	8.10	3.27		2.24	0.62	0.505	b.d.l.	1.52	0.299	0.1152	0.0012	0.11386	2.02	6.12
DB3C	0.87	0.98	0.57	2.23		0.44	0.34	0.004			0.036	0.11464	0.00082	0.11448	1.93	2.09
DB3CR				2.90	6.64	0.49	0.39	0.003	b.d.l.	2.11						
DB4B	1.20	0.88	4.37	3.30		2.48	b.d.l.	0.017	b.d.l.	0.43	0.018	0.11621	0.00006	0.11613	1.71	1.77
DB5C	1.21	0.40	0.59	0.63		0.08	0.10	0.022	b.d.l.	1.29	0.18	0.11564	0.00013	0.11486	1.88	3.05
DB6A	0.67	0.94	3.16	1.52		2.23	0.12	0.010	b.d.l.	0.93	0.014	0.11192	0.00057	0.11186	2.29	2.37
DB8A	0.71	0.61	0.80	3.80		5.03	b.d.l.	0.017	b.d.l.	0.40	0.10	0.11383	0.00005	0.11337	2.09	2.67
DB11AR				0.07	1.17	0.02	b.d.l.	0.015	b.d.l.	1.38						
Parry Peninsula Olivine separates																
DB1Aol			0.50	0.65		1.95	b.d.l.	0.028			0.27	0.12308	0.00056	0.12190	0.90	2.06
DB2Dol			0.00	0.00		0.07	b.d.l.	0.360								
DB2Eol			1.98	2.57		0.46	b.d.l.	0.011			0.028	0.11305	0.00003	0.11293	2.15	2.28
DB3Aol			0.66	1.48		1.04	b.d.l.	0.001			0.007	0.11293	0.00003	0.11290	2.15	2.18
DB4Bol			5.97	0.82		0.59	b.d.l.	0.039			0.032	0.11634	0.00003	0.11621	1.70	1.81
DB5Col			0.05	0.02		0.07	b.d.l.	0.046								
DB6Aol			4.40	2.21		1.58	b.d.l.	0.001			0.001	0.11187	0.00005	0.11186	2.29	2.30
DB8Aol			1.52	1.48		1.50	b.d.l.	0.001			0.002	0.1213	0.0022	0.12125	0.99	1.00
DB9Col			0.58	0.21		0.39	b.d.l.	0.018			0.15	0.11828	0.00004	0.11762	1.50	2.19
DB11Aol			0.16	0.22		0.07	b.d.l.	0.001			0.029	0.11449	0.00006	0.11436	1.95	2.08

Note: For HSE data, sample number ending with R represent the duplicate analyses done in the Universität Bonn, while all others were measured in the University of Alberta; all Se and Te data were measured in the Universität Bonn. Model ages (rhenium depletion age at the time of eruption ($T_{RDeruption}$) derived from ($^{187}Os/^{188}Os)_i$ by conducting the reduction of radiogenic ^{187}Os from ^{187}Re decay, and osmium model age (T_{MA})) are calculated relative to average ordinary chondrite ($^{187}0s/^{188}0s$= 0.1283, $^{187}Re/^{188}0s$=0.422; Horan et al., 2003). Eruptions ages for host kimberlites: central Victoria Island=271Ma and Parry Peninsula=270Ma.

Table 2. Summary of the CVI peridotite grouping based on the HSE characteristics

Group	Os (ppb)	Ir (ppb)	Os_N/Ir_N	Pt_N/Ir_N	Pd_N/Ir_N	Bulk Al_2O_3 (wt. %)	$^{187}Os/^{188}Os$	Number of samples
Group A	4.8-7.3	4.4-6.4	0.99-1.05	0.57-0.63	0.02-0.04	0.91-1.09	0.1130-0.1147	2 (SnO-27, -32)
Group B	2.4-3.9	2.5-3.9	0.90	0.25-0.37	0.16-0.24	1.63-1.87	0.1102-0.1133	2 (SnO-12, -21)
Group C	3.5-7.1	3.5-6.9	0.72-0.98	046-0.82	0.13-0.30	0.70-1.51	0.1135-0.1152	3 (SnO-15, -24, -33)
Group D	2.8-16.3	2.2-9.4	0.78-1.58	0.55-1.37	0.70-1.33	1.13-4.61	0.1140-0.1233	7(SnO-11, -17, -19, -20, -28, -34, -35)
Group E	0.4-1.0	1.8-2.3	0.18-0.50	0.02-0.19	0.02-0.34	0.88-2.00	0.1131-0.1152	2 (SnO-26, -36)

N: normalization to the chondrite values after Anders and Grevesse (1989) and Horan et al. (2003)

Table 3. FITPLOT parameters used for thermobarometry

Parameters	Crustal Heat Parameters	Slave Crustal Heat Parameters	Crustal Parameters with Lower Crust Heat Generation
Lower crust (km)	10	22	10
Upper crust (km)	18	23	18
Upper cust heat production (W/m^3)	1.2E-06	1.2E-06	1.2E-06
Lower crust heat production (W/m^3)	4.0E-07	4.0E-07	1.5E-07
Mantle heat production (W/m^3)	0	0	0
Central Victoria Island estimated diamond window (km)	119-215	118-219	117-215
Parry Peninsula estimated diamond window (km)	145-185	144-194	144-182

FITPLOTs provided in the text use crustal parameters, and the cases which use Slave crustal parameters and crustal parameters with lower crust heat generation are shown for comparison.